Design and Analysis of an Underwater Wedge Connection

Master's Thesis

Vivek Kurup

Faculty of Civil Engineering and Geosciences,
Delft University of Technology
September 2023

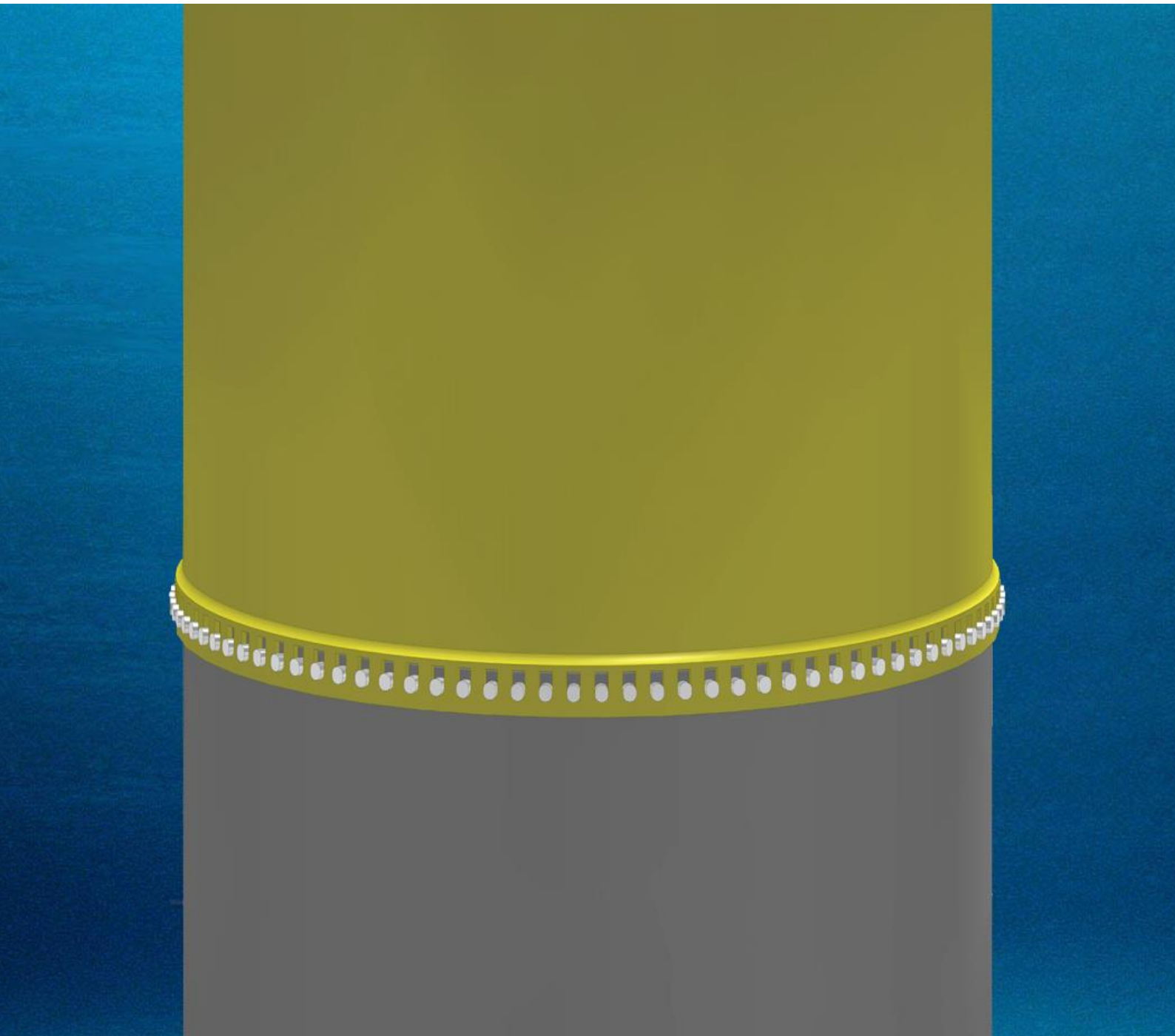

Design and Analysis of an Underwater Wedge Connection

By

Vivek Kurup

to obtain the degree of Master of Science
at the Delft University of Technology,
to be defended publicly on Tuesday September 26, 2023.

Student number:
5584396

Thesis committee:

Prof. Dr. Milan Veljkovic	TU Delft – Committee Chairperson
Dr. Trayana Tankova	TU Delft
Ir. Jeroen Hoving	TU Delft
Ir. Jasper Winkes	C1 Connections
Ir. Koen Creusen	C1 Connections

C1 CONNECTIONS

TU Delft

Abstract

The field of wind energy has experienced significant expansion and development driven by the need to reduce reliance on fossil fuels. Offshore wind turbines have become increasingly popular leading to larger turbines with greater energy output to match the growing demand. The most common foundation type of offshore wind turbines is the monopile foundation, consisting of two large diameter steel tubulars, the monopile (MP) and the transition piece (TP).

As wind turbine generators (WTGs) increase in size, the transportation and installation of MP foundations becomes more complex and expensive, requiring specialized vessels with adequate lifting capacity. This research investigates a new connection – the underwater wedge connection – as a method of connecting an MP to a TP underwater. By having an underwater connection, the size of the MP can be reduced as it no longer has to exceed the waterline.

The wedge connection consists of a dowel with an inclined plane and two flanges. A number of dowels will be placed around the circumference of the connection, fitted onto flanges on both the MP and TP. As the dowels are pushed into position, the inclined plane creates a vertical preload between the two flanges. This allows a tensile load on a segment of the connection (caused by the bending moment in the foundation) to be transferred to the foundation via two load paths: reduction of the preload, and by loading the dowel itself in shear.

First an analysis on the current state of art and relevant design codes was carried out. This analysis highlighted the requirements the connection needed to satisfy, in order to serve as starting points to make decisions regarding the design. The preliminary design of the connection is made using analytical calculations. The structural integrity of the flanges and the dowel at the Ultimate Limit State (ULS) was verified. A 3D model of the connection was then created to perform numerical analyses using ANSYS Static Structural. The behaviour of the connection under ULS and Fatigue Limit State (FLS) loading is studied. The opening and failure point of the connection along with the sensitivity of various parameters are also investigated.

The results show that connection was able to effectively transfer both tension and compression loads. The connection has a mechanical advantage of 1.95, meaning that it achieves the same preload as the ULS load by applying only 51.3% of the ULS segment load during installation. The connection opens gradually and only opens at a load higher than the ULS load. Even after opening, it continues to transmit loads effectively, with ultimate failure governed by the yielding of the lower flange. Additionally, the connection exhibits good fatigue resistance, with a low fatigue damage level of 3.8%.

It is recommended to conduct experiments to validate the numerical model employed in this study. Further studies should also be carried out to investigate the impact of structural imperfections on the behaviour of the connection.

Preface

This thesis marks the completion of my master's degree in Structural Engineering at the faculty of Civil Engineering and Geosciences at Delft University of Technology, the Netherlands. Before diving into my work I would like to take a moment to thank some people without whom this project would not have been successful.

Firstly I would like to thank my graduation committee. Prof. Dr. Milan Veljkovic, for his invaluable guidance and feedback throughout the project. Dr. Trayana Tankova, who always found time to have insightful conversations and provide constructive criticism which continuously motivated me. I also want to thank Jeroen Hoving, for his expertise and feedback which greatly contributed to this thesis.

I would also like to express my gratitude to everyone at C1 Connections for creating a welcoming workspace and setting up this enjoyable collaboration. Specifically, I want to thank Jasper, Koen, and George who always found time to answer questions and provide feedback. Thank you for giving me this opportunity and guiding me every step of the way.

I also want to thank my friends who provided support and encouragement throughout my time at TU Delft. To Achen and Amma, I wouldn't be here without you. To Shruthi, thank you for the constant support and encouragement. This thesis was possible not only through my efforts but also through the collective support and encouragement of all those who have played a vital role in my academic journey.

Table of Contents

List of Figures

List of Tables

1 Introduction

1.1 Background and Motivation

Driven by the need to reduce dependence on non-renewable sources of energy and to improve current renewable energy infrastructure, the offshore renewable sector has seen a recent boom in expansion and development. Wind energy is among the most popular renewable energy sources available. Wind turbines are the most popular method of harnessing this immense energy source. Initially, onshore wind turbines were the most popular variant however since the onset of the 21st century, offshore wind turbines have become increasingly popular. This is mainly due to the stronger, uninterrupted winds that can be accessed out at sea and reduced transmission constraints [1].

This growth has caused offshore projects to increase in scale, as Wind Turbine Generators (WTGs) and wind farms are required to increase their output in order to match this growth. Larger WTGs have greater available output as larger rotors can harness more energy. Hence, WTGS have increased in size over the years and are projected to keep increasing as demand rises, as seen in figure 1.1. As WTGs increase in size, so do all the elements that make up the structure. To support the weight of the heavier rotors, larger foundations are needed. This poses a challenge when transporting, lifting, shipping, and installing these structures out at sea.

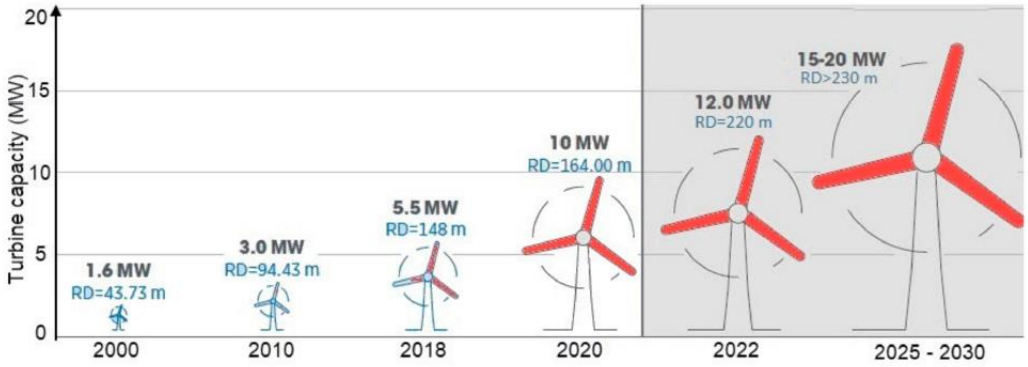

Figure 1.1: Power and rotor diameters of existing and planned offshore wind turbines [2]

A WTG has several components as shown in figure 1.2. The monopile (MP) is the main choice of foundation for offshore WTGs [3]. Other foundation structures include the gravity foundation, suction caisson foundation, tripod and jacket foundations [4]. The MP is the most economical choice for WTG foundations at water depths of 50m or less and sand gravel-type seabeds [4]. The MP is also easily applied in North Sea offshore developments where the soil is predominantly gravel and sand. The components of a typical offshore WTG with a monopile foundation are shown in figure 1.2. Another component of a WTG is a transition piece (TP) which connects the foundation to the tower structure. The TP has several functions such as distributing loads from the tower structure to the foundation, as a connection interface between the tower and the substructure and housing for access platforms and cable routing systems.

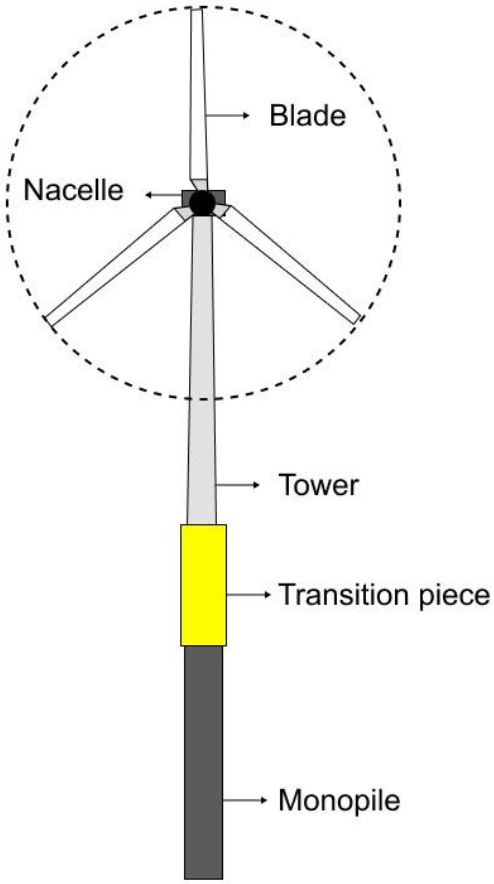

Figure 1.2: The components of a WTG with a monopile foundation [5]

A commonly realised solution to connect the MP to the TP is through above-water bolted connections such as the ring flange connection. With an above-water connection, the MP has to be long enough to exceed the waterline. The MP is often much longer, and thus, much heavier than the TP. As the size of WTGs increases, so do the MPs making it challenging to transport, lift and install. As MPs get larger with time, there is more demand for vessels that can lift and install them – increasing overall costs.

As this growth is only expected to accelerate in the coming years, the installation capacity of vessels is at risk of becoming the limit of foundation sizes which can be detrimental to the development of offshore wind farms. This presents an avenue for research – reducing the sizes of MPs to lower overall costs by reducing the demand on vessels and lifting equipment. By having an underwater connection between the MP and the transition piece, the size of each MP can be greatly reduced.

1.1.1 Principles of the wedge and the inclined plane

The connection will use the principle of the wedge, which combines the use of two classical simple machines: the inclined plane and the wedge. The plane allows for the transformation of a horizontal force into a vertical force. A simple inclined plane is shown in figure 1.3.

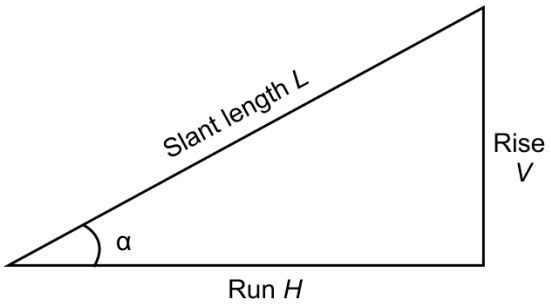

Figure 1.3: The inclined plane [6]

The degree of magnification of the horizontal force is dependent on the angle of slope, α and friction across the surface. This is quantified as the mechanical advantage of the inclined plane, which is shown below in equation 1.1.

$$MA = \frac{F_{vertical}}{F_{horizontal}} \tag{1.1}$$

The underwater wedge connection uses the inclined plane to generate a vertical preload between the flanges of an MP and TP by transforming a horizontal actuation force.

1.1.2 The C1 wedge connection

The underwater wedge connection is inspired by the above-water C1 wedge connection. The C1 wedge connection uses the same principle of the inclined plane to form a connection between a MP and TP. Development of this connection started due to the challenges surrounding the design and installation of conventional L-flange connections with higher capacity [7]. This is a symmetrical connection between two tubular sections with a small, horizontally placed a bolt that pull two wedges together [8]. The connection features two flanges – an upper flange that is fork-shaped and slides over a cylindrical lower flange, as shown in figure 1.4. Radially elongated holes that are present around the circumference of both these flanges allow the fastener assembly to be placed inside. The fastener assembly generates a vertical preload which pulls the two flanges together. The wedges use the inclined plane principle which allows the horizontal bolt force to be transformed and magnified as a vertical preload between the flanges by pulling them together.

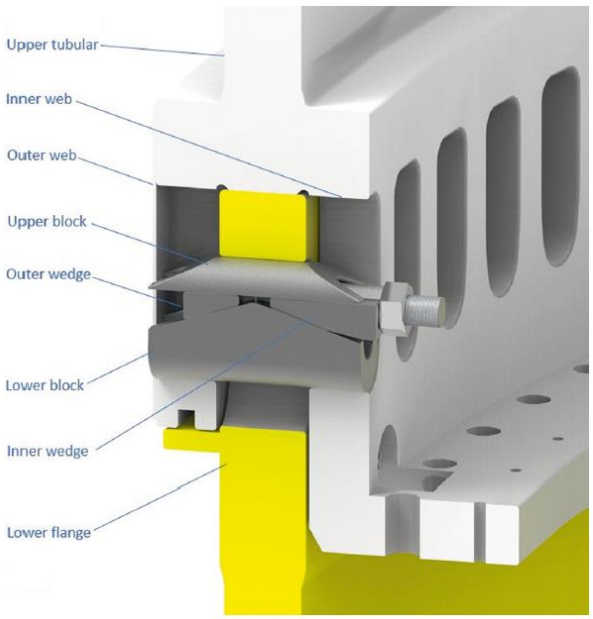

Figure 1.4: The main components of a C1 Wedge Connection [8]

The main concern with the C1 Wedge connection design for underwater applications is that currently, a bolt needs to be pretensioned to create the preload. This aspect of the design is challenging to implement underwater, as torquing the bolt at such depths of water would require remotely operated vehicles (ROV) or deep-sea divers. This is considered unfeasible. Furthermore, the design's corrosion resistance would also have to be improved, keeping in mind the constant contact with seawater.

1.2 Aim and Research Questions

The aim of this project is to design an underwater connection of a WTG support structure. This is achieved by setting the objectives to study whether the connection can be made by using the principle of the wedge and to investigate the structural behaviour of this connection under ULS and FLS loads. The main drivers of this project can be seen in the research questions defined below:

1. What are the requirements the underwater wedge connection should satisfy?
    i. How to protect the connection against corrosion?
    ii. What in-service maintenance and service requirements would the design have to satisfy?
2. How does the connection behave under ULS loading?
3. How does the connection behave under FLS loading?

1.3 Methodology

Firstly, a literature review was performed to analyse the state of the art in the field of connections in wind turbine support structures. Current solutions for connections above and underwater, along with other subsea engineering solutions for steel connections in the submerged zone, were critically evaluated.

For the design phase, a combination of semi-empirical design methods was adopted. This allowed requirements from design codes to serve as starting points to make early decisions concerning the

design. This analysis highlighted the requirements the connection needed to satisfy, in order to address the first research question of this project.

The requirement analysis was followed by the preliminary design of a connection through an analytical calculations. By the end of this phase, initial design dimensions and parameters were fixed. This preliminary design served as the starting point for the structural analysis through finite element analysis (FEA).

The project then moved on to the final phase, which was the structural analysis of the preliminary design. This was done using numerical modelling and FE analysis to analyse and possibly compare the designs. This allowed for the examination of complex structural behaviour beyond the limits of analytical models. The installation process and behaviour under ULS loading were investigated, observing the opening of the connection or the point of structural failure. Finally, an initial fatigue assessment of the connection was conducted using the Markov Matrix approach.

1.4 Design Loads

The design loads at the connection level are shown in Table 1.1.

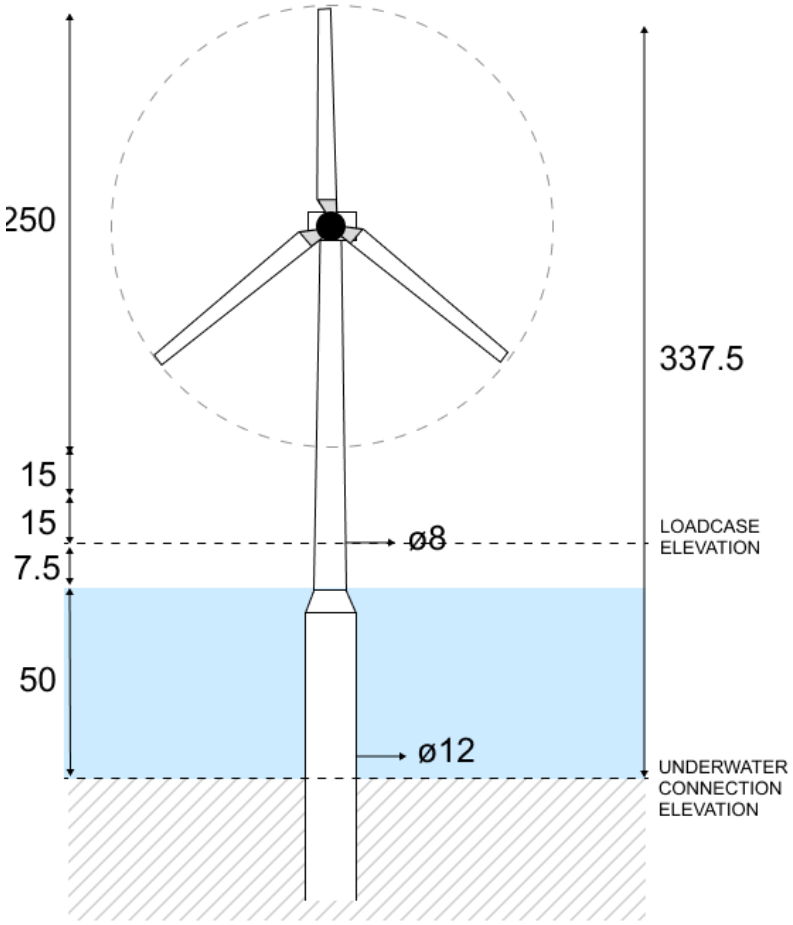

Figure 1.5: WTG dimensions

Table 1.1: Dimensions and Design Loads at the connection

Specification	**Value**
Rotor diameter	250m
Rotor clearance	15m
Distance between nacelle and WL	162.5m
Distance between nacelle and load case elevation	155m
Load case elevation to WL	7.5m
Depth of water	-50m
Connection diameter	12m
Connection wall thickness	150mm
Design bending moment at connection	1232.5 MNm
Design line load at the connection	10.90 MN/m

For the purpose of this investigation, it is assumed that the connection will be loaded primarily from wind loading. Wave loading is assumed to be of an order of magnitude lower than the wind load and is neglected. The calculation of the scaled loads are provided in Appendix A: ULS and FLS load calculations.

2 State of Art

In this chapter, a review of the current solutions for MP to TP connections is presented. In addition to this, a study of the practices for steel-steel connections in subsea engineering projects will be carried out to better understand the challenges when working with steel in an underwater environment. After the introduction of each solution, its benefits and applicability to the current problem of this thesis is discussed. This is done to assess the current state of art and highlight the current challenges faced in this field. This provides valuable input for the design of the wedge connection.

2.1 L-Flange bolted connections

Bolted connections feature in several steel structures as a common connection method. They are the industry standard used in offshore WTGs MP-TP connections, a typical connection can be seen below in figure 2.1. The major benefit bolted connections offer is that they are easy to design with a very standardized process. Tensile loads that arise from the bending of the tower are transferred through the prestressed bolts and the upper and lower flange, meanwhile, the compressive loads are transferred directly via the flanges [9].

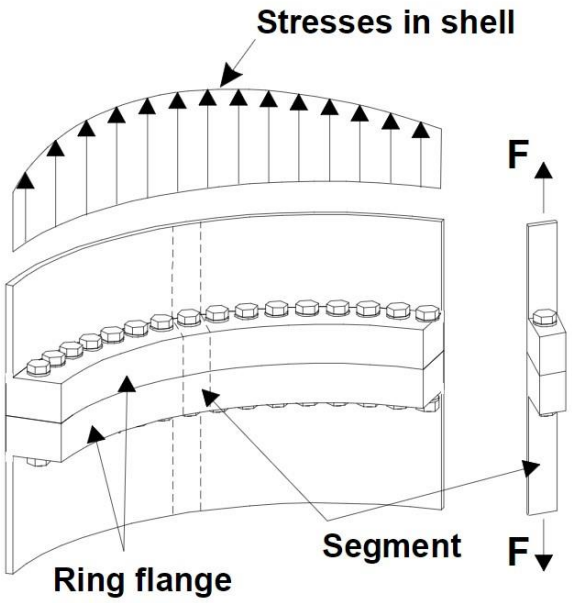

Figure 2.1: Components of the L-flange bolted connection

L-flange connections often feature very large bolts as they must be highly preloaded to ensure sufficient capacity for ULS and FLS design. As the size of WTGs increases, larger bolts are required to ensure a safe design, with recent designs requiring bolt sizes up to M80 along with thicker and wider flanges [8]. This shows that the L-flange connection doesn't scale well with the ever-increasing demand. It also highlights health and safety issues as bolts greater than M64 and the torquing/tensioning tools for bolts of such size are beyond the safe limits of allowable lifting weights [10].

2.2 Grouted connections

The grouted connection has been the standard manner of connecting MP-TP for WTG along with the L-flange bolted connection. The connection consists of the TP mounted concentrically on the MP which has been driven onto the seabed [11]. The space between the concentric rings is then filled with specially developed grout which settles into high-strength concrete. The grout transfers the loads from the TP to the MP enabling it to withstand the large bending moments faced by the WTG. The amount of resistance is proportional to the overlap length between the TP and MP, also known as the grout length.

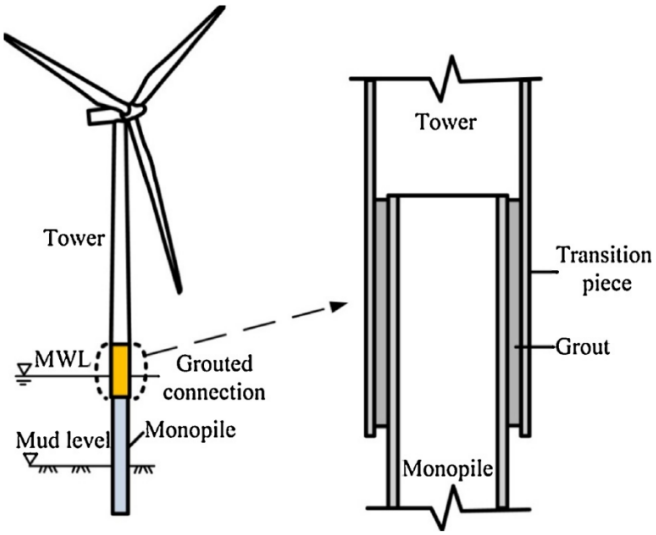

Figure 2.2: Components of an underwater grouted connection [12]

As the MP and TP deform radially under the bending moment, they can cause the degradation of the grout due to the relative sliding of the surfaces against the grout. The bending moment causes a tension load in the circumferential direction which could exceed the tensile capacity of the grout [13]. A primary concern of a grouted connection is the brittle behaviour of the grout. This can lead to sudden settlements of towers with little warning beforehand. To provide additional resistance to shearing in the connection, shear keys have been placed in several grouted connections.

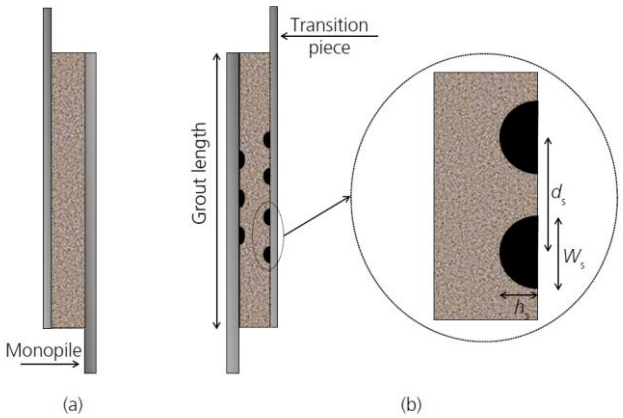

Figure 2.3: Grouted connections (a) without and (b) with shear keys [11]

Although the shear keys provide additional resistance, they have a drawback as they introduce stress concentrations around the welds on the steel surface. This reduces the lifetime estimation of the

structure or requires heavier sections to be designed without shear keys [14]. They also have a poor level of workability as the curing and settling process of the grout requires a lot of time and provision. This process can lead to increased delays as the installation is restricted by the weather and sea conditions.

2.3 Slip Joint

Due to the issues with typical grouted connections, a recent alternative connection method is the slip joint. The slip joint features two conical steel sections one of which is attached on top of the MP and the other at the bottom end of the TP. They are dimensioned such that the two sections fit closely with each other similar to two inverted cups [15]. In April 2020, the first full-size connection was installed in the Borssele Site V offshore wind farm [16].

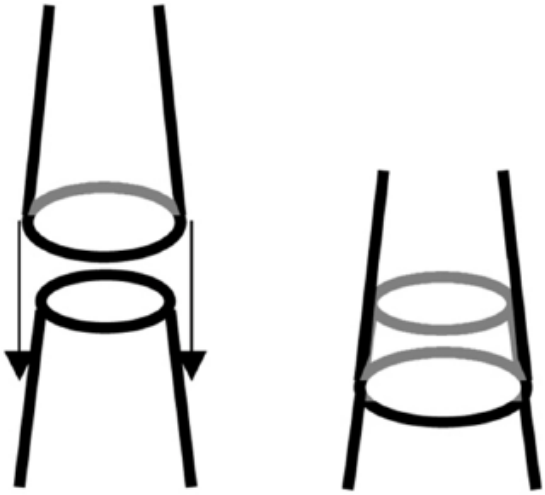

Figure 2.4: Concept of the slip joint [15]

The load is transferred from the TP to the MP through friction and normal contact forces, which arise primarily due to the self weight of the overall structure and the bending moments arising through the WTG operation [17].

2.4 Underwater bolted connections

Bolted connections are not limited to above-water scenarios only. They are also widely used as the connection method for segments of steel plates and shells for various other underwater and subsea engineering applications. This is mainly because bolted flange connections can offer large cost savings between segments of undersea pipelines and other subsea structures [18].

Figure 2.5: Underwater pipelines in the seabed with bolted flange connections [19]

Repeated failures of bolted assemblies over the years triggered the Bureau of Safety and Environmental Enforcement [20] to issue a safety alert and the DNVGL to publish a *Study on Bolt Incidents* in 2019 [21]. Studies due to this were performed by Ripsch and Henkel [22] to observe the behaviour of bolted connections that were assembled in the splash and submerged zones. It was found that bolts assembled in these regions were more susceptible to loss of preload and bolt overload. Furthermore, torque-based tightening could not ensure a sufficient level of bolt preload above design preload level, increasing the risk of self-loosening.

Bolt relaxation remains a major challenge due to the lack of possible regular maintenance and inspection. Bolt relaxation is affected by elastic interactions, embedment, static and cyclic loading and long-term relaxation or creep [23]. In addition, experiments carried out also indicate a relation between the thickness and selection of coating material for the bolt assembly and the subsequent loss of preload. Uncoated plates suffer from lower preload losses compared to cases with coated plates, which could be counterproductive in the high-corrosive submerged region.

2.5 Underwater welding

Underwater welding has been a solution for subsea engineering projects in recent years when it comes to fabrication and underwater repairs for submerged steel structures. Underwater welding can be classified into three major types [24]:

- Wet welding:
  This method involves welding without a barrier between water and the welding arc, often performed by deep-sea welder divers. While it allows for welding complex structures, the rapid cooling in water reduces weld and heat-affected zone ductility, leading to high porosity [25].

- Local cavity welding:
  This approach uses standard equipment with a special nozzle and cover, offering conditions similar to welding in air, resulting in better quality welds.

- Dry welding:
  Dry welding takes place in a water-free chamber, ensuring welds of similar quality to those above water. However, the creation of this chamber increases associated costs.

Underwater welds typically exhibit lower quality and mechanical properties due to factors such as rapid cooling, high pressure, and hydrogen content in the weld metal [26]. These issues include increased porosity, hot and cold cracks, slag entrapment, and changes in chemical composition.

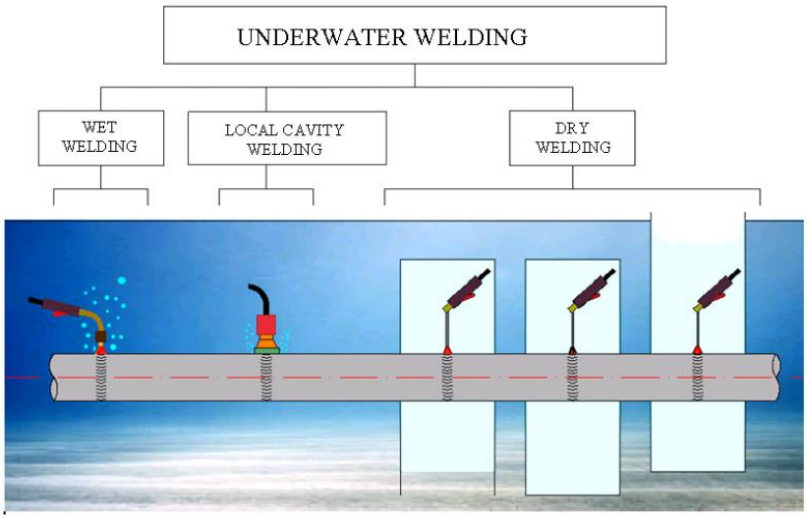

Figure 2.6: Different types of underwater welding [24]

2.6 Discussion of the state of art in connection technology

This state of art analysis sheds light on the advantages and limitations of various offshore MP-TP connection methods, especially in underwater applications. It is evident that each method carries its own set of benefits and drawbacks, and the selection of an appropriate connection method is critical to the success and longevity of offshore WTG installations. Bolted connections, while well-established and widely used above water, pose challenges when implemented underwater. They are sensitive to preload loss and require regular inspection and maintenance, which can be cost-intensive. Additionally, as the size of WTGs increases, bolted connections may become less practical due to scalability issues.

Grouted connections offer an alternative standard method for MP-TP connections underwater. However, they demand a substantial amount of steel to ensure a proper overlap, increasing overall costs. Moreover, the brittle failure of grout can result in sudden settlements of WTGs, impacting their structural integrity. The curing process of grout further complicates workability. Slip Joint connections is another focus of research, with the advantage of easy installation and the potential for underwater implementation. They address many of the issues associated with grouted connections, making them a viable option. However, they still require a considerable amount of steel to ensure sufficient overlap between the MP and TP, which may add to overall project costs. In contrast, underwater welding is found to be unsuitable for MP-TP connections due to issues related to overall quality, increased brittleness, and porosity. These drawbacks make underwater welding an impractical choice, especially when considering the thicknesses of the MP and TP sections.

Considering the limitations identified in the comparison, it is evident that the design of the underwater wedge connection must prioritize ease of installation, inspection, and scalability, particularly with larger WTG diameters. The goal should be to create a connection method that can be easily installed, minimizing the need for frequent and costly inspections. Additionally, it must exhibit robust ULS and FLS resistance to ensure scalability with larger WTGs.

3 Design Requirements

In this chapter, an analysis of the current relevant design recommendations and standards is carried out. This is to highlight the requirements the wedge connection should satisfy prior to the design phase. In this review, the requirements relating to; protecting the structure against corrosion, in-service inspection, maintenance and monitoring and material selection are examined using the design codes shown in Table 3.1.

Table 3.1: Design standards and recommendations reviewed

DNV-RP-0416: Corrosion protection for wind turbines [27]
DNV-ST-0126: Support structures for wind turbines [28]
EN 1993-1-4: General rules- Supplementary rules for stainless steels [29]
DNV-OS-C101: Design of offshore steel structures, general-LRFD method [30]

3.1 Corrosion protection

The underwater environment, in which the connection will be implemented, will naturally be highly corrosive for steel structures. The environment surrounding the substructure can be defined in terms of 4 zones, as seen in figure 3.1. The connection will be made in the submerged zone and there are several requirements structures within this region must satisfy [27].

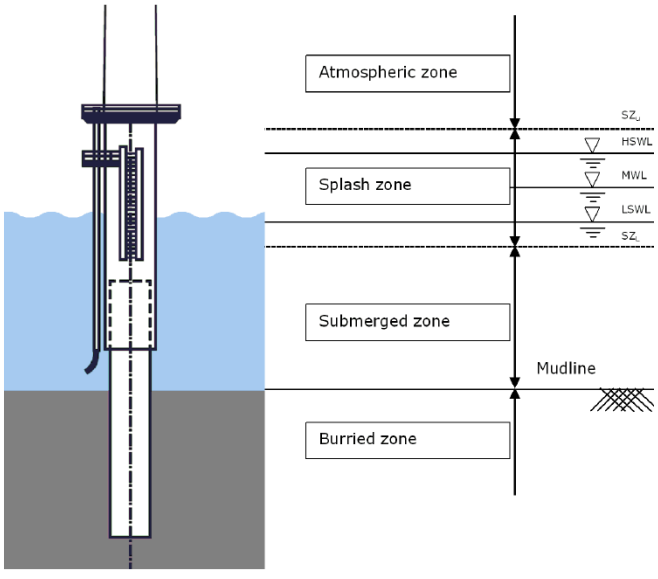

Figure 3.1: Schematic representation of levels and zones in sea water environment [27]

Corrosion protection requirements state that it is mandatory that external surfaces of the submerged zone shall have cathodic protection (CP). The use of coating is optional, primarily to reduce the required CP capacity. It is required that structural elements within submerged zone are equipped with CP along with possible coating that can reduce the demand on the systems [27].

There exists two main methods for CP; sacrificial anode systems and impressed current systems. There are benefits and drawbacks to either system, which are presented in Table 3.2 below based on the Guidance Notes on Cathodic Protection of Offshore Structures [31].

Table 3.2: Comparison between Sacrificial Anode systems and Impressed Current Systems [31]

Comparison item	Sacrificial Anode Systems	Impressed Current Systems
Cost	Simple design and installation. No maintenance, but costly to replace anodes.	Higher initial cost, lower life-cycle cost. Regular maintenance required.
Consequence of anode damage	Loss of a few anodes has little effect.	Critical to system effectiveness.
Environment effect on cathodic protection efficiency	Practical for low electrolyte resistivity, like seawater. Uncontrollable potential and current.	Less restricted by resistivity. Controllable potential and current.
Detriment to coating and steel	Coating system is selected to resist cathodic disbonding.	Can over-polarize and harm coatings.
Power source	No electric power needed. Suitable where power is unavailable.	Requires continuous DC power supply.
Interaction	Less likely to affect any neighbouring structures.	Effects on nearby structures need assessment.

Based on the available literature, sacrificial anode systems are more practical and feasible to be incorporated within the connection system. The corrosion behaviour of the connection itself is also a matter of possible experimentation and future studies, which will not be covered within this project.

3.2 In-service inspection, maintenance and monitoring

As mentioned in previous chapters, another concern is the amount of inspection and maintenance that can be carried out. With limited access for these activities, it is pivotal that the current design code requirements are reviewed to understand how these challenges can be overcome.

The design standards states that a wind turbine support structure is typically planned for a design lifetime of 20 to 30 years [28]. In order to sustain the impact from power production and from the environment, adequate inspection and maintenance shall be carried out for the support structures.

Where inspection is not possible or practicable, the structures shall be designed and constructed so that adequate durability for the entire operating life of the installation is assured. A typical periodical inspection for an offshore structure can consist of:

- general visual inspection
- close visual inspection
- non-destructive examination
- destructive testing
- instrumentation-based condition monitoring

For offshore structures general visual underwater inspections can be carried out using a ROV, whereas close visual underwater inspections could require inspections carried out by a diver. These operations are likely to be very expensive and unfeasible to be carried out in a periodical basis. Therefore, the best approach would be to ensure that the design of the connection will last the full design lifetime of 30 years without any inspection [28].

3.3 Material Selection

Bimetallic corrosion is liable to occur when dissimilar metals are in electrical contact in any electrolyte [29]. In addition, introducing two metals that have a large difference in electrochemical potential will likely cause one of the metals to become an anode, causing extensive corrosion damage [32]. The use of stainless steel dowels with carbon steel flanges for example, is unlikely to cause additional corrosion within the dowel but can cause additional corrosion within the flanges. This is because there is a difference in electrochemical potential between the two metals, as seen in figure 3.2 below.

Therefore, the connection will be made entirely of structural steel. The grade is chosen to match that of the tower structure to avoid the introduction of dissimilar metals in the corrosive environment. Structural steel is commonly used in offshore and underwater application and displays good structural performance in terms of yield strength and tensile strengths. Materials such as stainless steel could offer improved corrosion resistance for the dowel itself. However, it might promote bimetallic corrosion and crevice corrosion at the interfaces between the dowel and flanges.

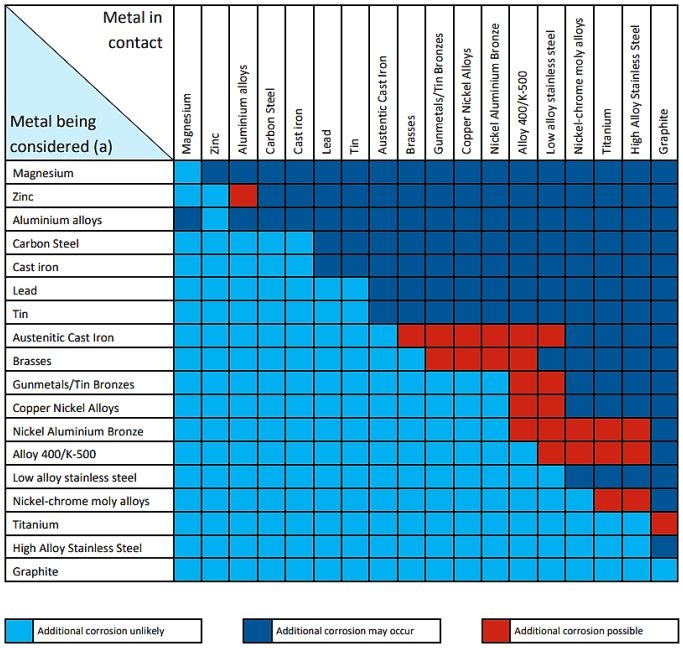

Figure 3.2: Risk of additional corrosion through bimetallic contact in neutral aqueous electrolytes [33]

4 Principles of the Connection

In this chapter, an introduction to the principles behind the underwater wedge connection is presented. Analytical expressions will be derived to describe the load transfer, mechanical advantage, self-locking and the expected vertical preload in the connection. Aside from this, friction between the contact surfaces of the connection is also an important part of the design. A brief overview of the theory of friction is shown, followed by a discussion of the available friction coefficient values in the literature that are of relevance to this connection.

4.1 Concept introduction

The wedge connection uses the principle of the inclined plane to generate a vertical preload between the flanges of the connection. The inclined plane is introduced through the wedge or in this case, a dowel. The dowel is inclined under a specific angle. The connection needs to be self-locking to ensure that after the horizontal load applied is removed, the dowel stays in position.

4.1.1 Components of the connection

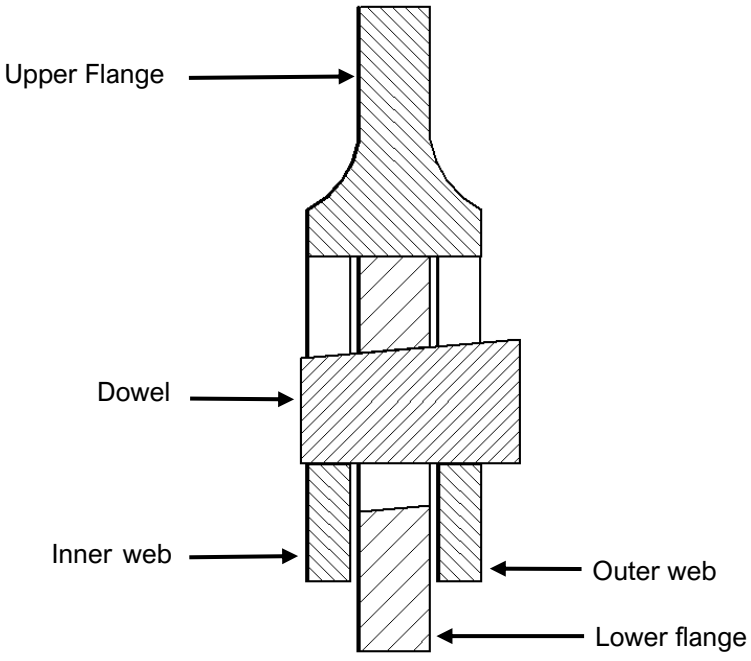

Figure 4.1: Components of the connection

The connection features an upper flange with a fork shaped cross section, a cylindrical lower flange and an angled dowel that is fastened into the assembly. The lower flange is attached onto the MP and the upper flange onto the TP of a WTG.

4.2 Load paths in the connection

Similar to bolted connections, the wedge connection can be preloaded to transfer external loads more efficiently. Preloading the connection increases the contact stress between the two flanges. This effectively increases the overall stiffness of the connection. This is because the assembly of the preloaded connection is like that of a spring system of 2 different stiffnesses loaded in parallel. The combined stiffness is greater than the stiffness of any individual spring in the parallel arrangement. This increased stiffness creates a more rigid and stable connection that can better withstand the forces and loads experienced in offshore environments.

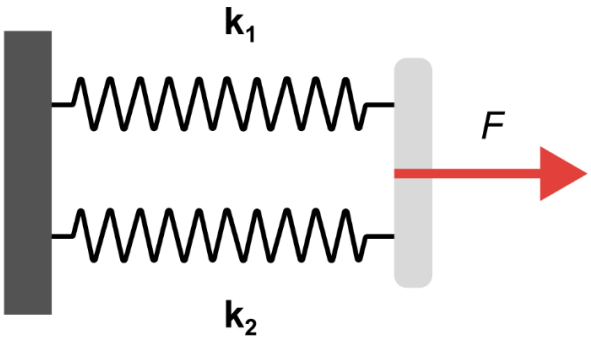

Figure 4.2: Equivalent spring system

The wedge connection uses two mechanisms to transfer external load. The primary load path is through the preload between the flanges of the connection. Compression only has one load path and is transferred directly from the upper flange to the lower flange. This increases the contact stress between the flanges. The primary load path for tensile loads is by reduction of the preload between the flanges. If preload is not present tensile loads are transferred from the webs of the UF, through the dowel and then to the lower flange.

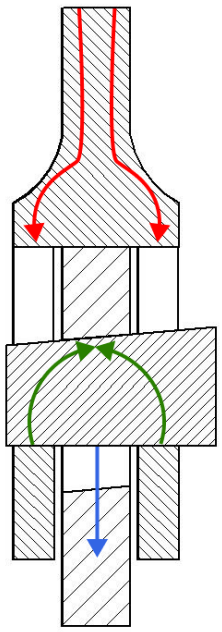

Figure 4.3: Load path without preload for tensile loads

4.3 Friction between the contact surfaces

Friction, the force resisting the relative motion of surfaces sliding against each other can be expressed as:

$$F_s = \mu * F_N \tag{4.1}$$

F_s is the force sufficient to prevent relative sliding of the bodies.

F_N is the force normal to the interface between the bodies .

μ is the friction coefficient

Friction coefficient is the ratio of two forces acting, respectively, perpendicular and parallel to an interface between two bodies under relative motion or impending relative motion. The friction coefficient that represents the friction opposing the onset of relative motion (impending motion) is the static coefficient of friction while the dynamic coefficient represents the frictional force between two surfaces in relative motion [34]. As the static behaviour of the dowel in the connection is of interest, static friction coefficient will be used for the contact surfaces.

There are many factors that affect the coefficient of friction including the material of the bodies, environment, applied forces, presence of lubricants and coating and etc. Therefore, the selection of friction coefficient must reflect the environments its applied in. Available literature provides a range of friction coefficients for steel to steel contact surfaces. They are summarised in table 4.1 below.

Table 4.1: Friction coefficients for steel to steel contact surfaces

Materials	**Coefficient of Static Friction**	**Source**
Steel - Steel	0.74	CRC Handbook of Physical Quantities. (1997) [35]
Flat machined Steel - Steel	0.19	Nolle, H., & Richardson, R. S. H. (1973) [36]
Steel - Steel (Untreated surfaces)	0.2	DNV-OS-C101 [30]
Rusted – Rusted Steel in air	0.59-0.73	Pijpers, R. J. M., & Slot, H. M. (2020) [37]
Coated – Coated Steel in air	0.05-0.15	
Rusted – Rusted Steel in seawater	0.51-0.69	
Coated – Coated Steel in seawater	0.08-0.15	

In general, design guidebooks suggest friction coefficients around 0.74 for steel to steel surface contact [35]. Studies into flat machined steel surfaces instead showed lower coefficients of 0.19 [36]. This closely matches the value suggested by the DNV codes of 0.2 for untreated steel surfaces. The challenge is that the above values have been obtained for in air interaction, whereby the presence of seawater in the underwater connection can affect the friction. Experiments performed by TNO and TU Delft

performed in artificial seawater showed a coefficient of friction below 0.2 while steel with rusted surfaces showed a range between 0.51 and 0.69. Friction between the contact surfaces is assumed to be 0.2 for this study, however more experiments need to be carried out in similar environment to understand frictional properties better.

4.4 Load transfer mechanics

The free body diagrams (FBD) of the connection is shown below in Figure 4.4 and Figure 4.5.

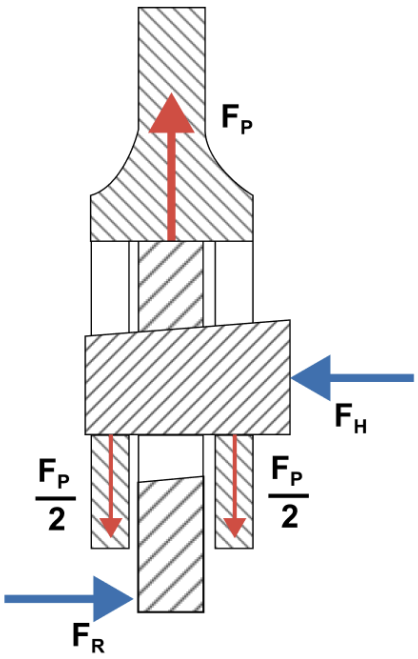

Figure 4.4: FBD of MP and TP

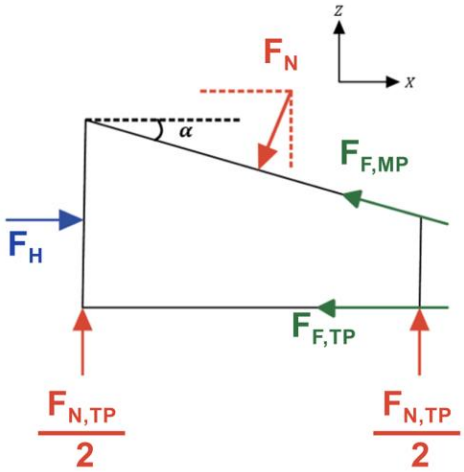

Figure 4.5: FBD of dowel during installation

The equilibrium equations for the dowel can be calculated as shown below:

$$\sum F_X = 0$$

$$F_H - F_{F,MP} * cos\,\alpha - F_{F,TP} - F_{N,MP} * sin\,\alpha = 0 \tag{4.2}$$

$$\sum F_Z = 0$$

$$F_{N,TP} + F_{F,MP} * sin\,\alpha - F_{N,MP} * cos\,\alpha = 0 \tag{4.3}$$

4.5 Mechanical advantage of connection

Based on the definition of friction (4.1) the value for friction along the TP and MP interfaces can be defined as:

$$F_{F,TP} = \mu * F_{N,TP} \qquad F_{F,MP} = \mu * F_{N,MP}$$

Substituting these into (4.3):

$$F_H = F_{N,MP}(\sin\alpha + \mu\cos\alpha) + \mu * F_{N,TP}$$

And substituting into (4.2):

$$F_{N,TP} = F_{N,MP} * \cos\alpha - \mu * F_{N,MP} * \sin\alpha$$

The force perpendicular (normal) to the inclined plane is then defined as:

$$F_{N,MP} = \frac{F_{N,TP}}{\cos\alpha(1 - \mu * \tan\alpha)}$$

From the two free-body diagrams, the amount of vertical preload generated between the two flanges can be expressed in terms of the normal force between the dowel and TP.

$$F_{N,TP} = F_P = F_{N,MP}(\cos\alpha(1 - \mu * \tan\alpha))$$

The normal force generated with the application of a certain horizontal preload on the dowel is:

$$F_{N,MP} = \frac{F_H}{(\sin\alpha + 2\mu\cos\alpha - \mu^2\sin\alpha)}$$

The mechanical advantage of the connection can then be found:

$$MA = \frac{F_P}{F_H} = \frac{\cos\alpha(1 - \mu * \tan\alpha)}{(\sin\alpha + 2\mu\cos\alpha - \mu^2\sin\alpha)} \tag{4.4}$$

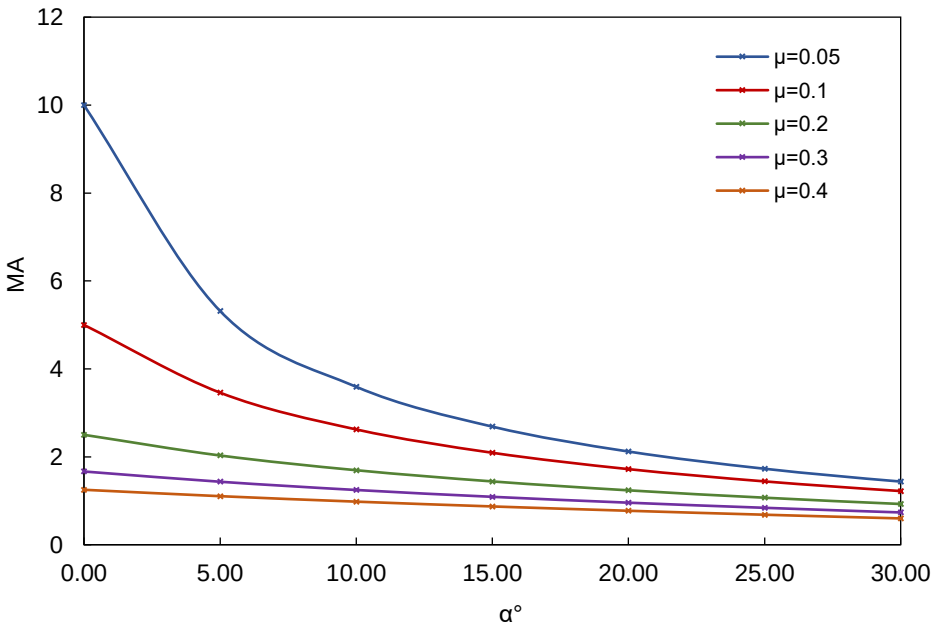

Figure 4.6: Mechanical advantage vs dowel angle for various friction coefficients

It can be seen that from the figure above that there is a clear advantage in having a lower friction of coefficient as less energy is lost due to friction. A smaller dowel angle also results in a larger mechanical advantage.

4.6 Self-locking of connection

As the connection relies on the dowel being in position to ensure that the vertical preload generated between the flanges does not reduce, it is important that the dowel stays in place and remains self locking even after the removal of the applied horizontal preload. The FBD of the connection for the situation when the horizontal preload, FH is removed is shown below. The direction of the frictional forces along the dowel interfaces now change direction as they now keep the dowel in place.

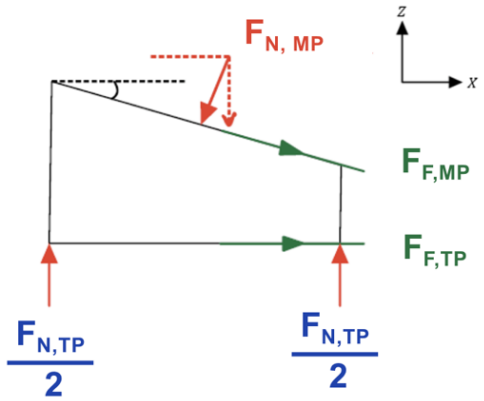

Figure 4.7: FBD of dowel without the presence of horizontal preloading force

The new equilibrium equations can be formulated as below:

$$\sum F_X = 0$$

$$F_{N,MP} * \sin\alpha - F_{N,MP} * \mu * \cos\alpha - F_{N,TP} * \mu = 0$$

$$\sum F_Y = 0$$

$$F_{N,TP} - F_{F,MP} * \sin\alpha - F_{N,MP} * \cos\alpha = 0$$

$$F_{N,TP} = F_{N,MP}(\cos\alpha + \mu * \sin\alpha)$$

The two parameters that affect the self-locking are the dowel angle and the friction coefficients between the surfaces. By substituting the vertical equilibrium into the horizontal equilibrium equation, the force terms can be removed and an expression of the dowel angle in terms of the friction coefficient can be found (4.5). This relationship is shown graphically in Figure 4.8.

$$\alpha = \arctan\left(\frac{2\mu}{1-\mu^2}\right) \tag{4.5}$$

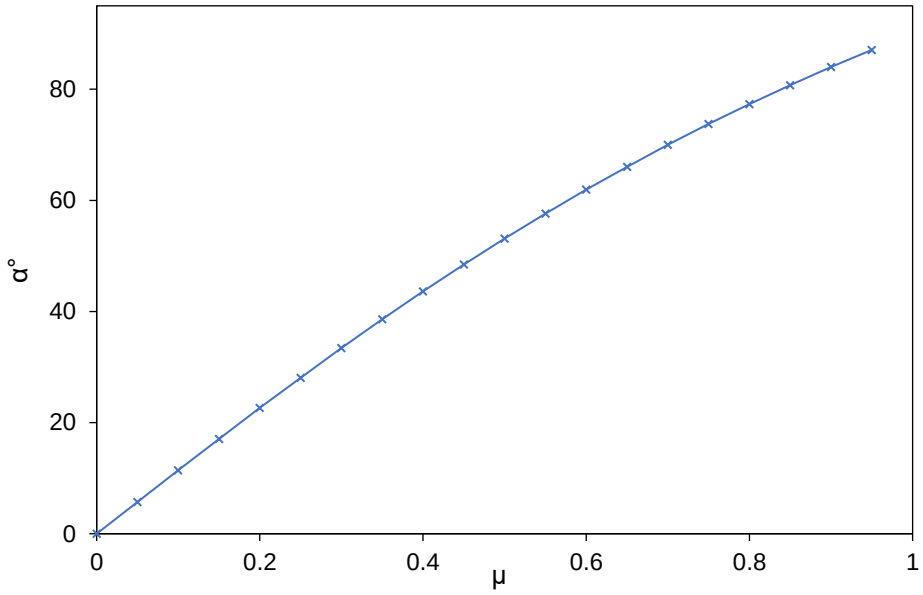

Figure 4.8: Self locking angle vs friction coefficients

A lower friction coefficient corresponds to smaller allowable wedge angles that ensure self locking. The friction coefficient selected for the dowel corresponds to standard steel-steel contact based on the literature in section 4.3 of μ = 0.2. The dowel angle selected is 5°.

4.7 Vertical preload generation

The key principle behind the wedge connection is that the horizontal preload applied onto the dowel is transformed and magnified into a vertical preload between the flanges of the connection.

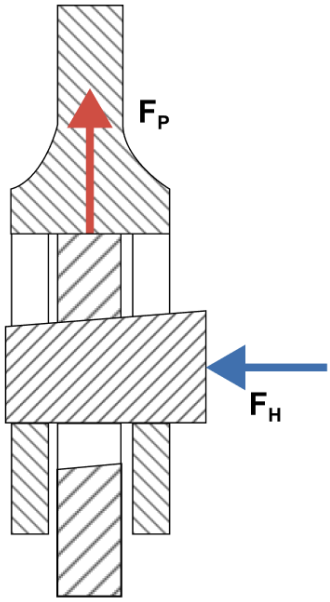

Figure 4.9: Preloading mechanism in connection

The relationship between the horizontal and vertical preload based on the mechanical advantage (4.4) can be written as and plotted in the graph below:

$$F_P = F_H * \frac{\cos\alpha(1 - \mu * \tan\alpha)}{(\sin\alpha + 2\mu\cos\alpha - \mu^2\sin\alpha)}$$

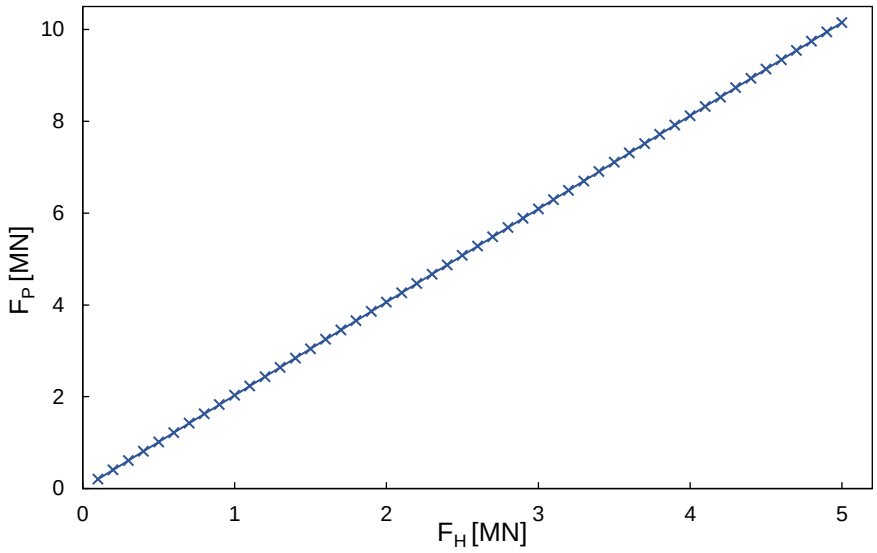

Figure 4.10: Applied horizontal preload vs Vertical preload between flanges

For a dowel angle = 5° and friction coefficient μ=0.2 the mechanical advantage is 2.03. The horizontal preload applied onto the dowel is magnified by a factor of 2.03 into the vertical preload between the flanges.

5 Preliminary Design

In this chapter, the process by which a preliminary design of the connection is created will be outlined. This is done through analytical calculations. The preliminary design will then be modelled in 3D using computer aided design (CAD).

5.1 Design assumptions

For the hand calculations the following assumptions are made:

- Assuming the use of S355 steel for the design and a linear stress-strain relationship is considered for the applied loads.
- Euler bending theory is valid to describe the bending of the dowel.
- Effects of imperfections and waviness is not considered.

5.2 Ideal size

The ULS resistance of the Wedge Connection is governed by the wall thickness of the LF and the webs of the UF. Two factors are considered: the net stress between the holes and the contact pressure in the holes.

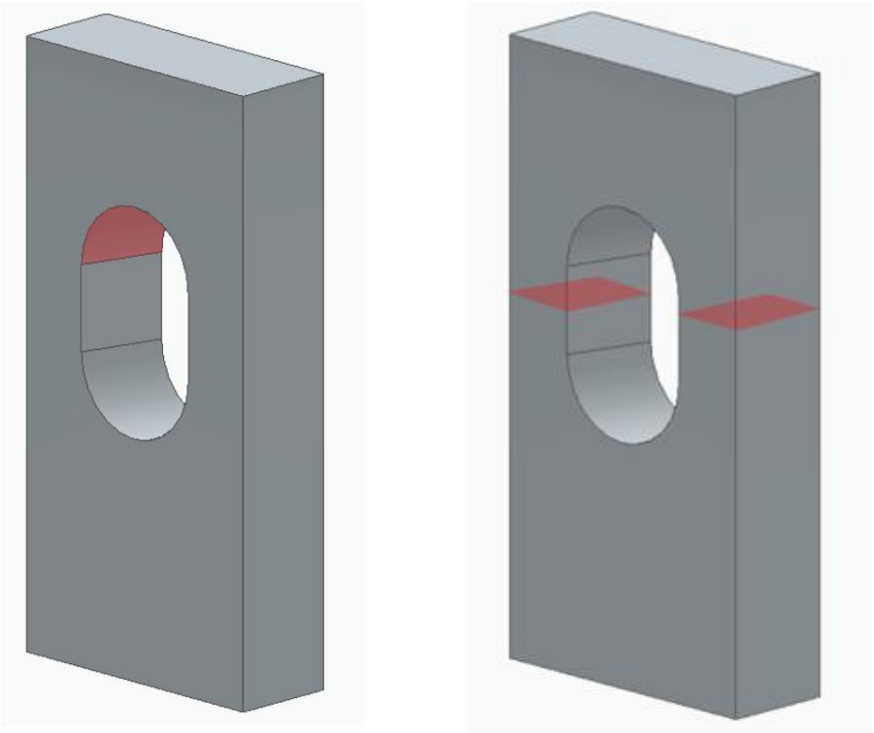

Figure 5.1: Contact pressure (left) and net stress (right) in the lower flange segment

The equal utilisation of these two stresses is the starting point for finding the ideal segment length for the connection.

Net Area:

$$A_{net} = t * (l_{seg} - d_{hole})$$

Net Stress:

$$\sigma_{net} = \frac{F_{seg}}{A_{net}} \leq \frac{f_y}{\gamma_{M1}}$$

Where: $\gamma_{M1} = 1.1$ (the partial safety factor for the resistance of members and cross-sections [38])

Projected Area:

$$A_{projected} = t * d_{dowel}$$

Contact pressure:

$$\sigma_{contact} = \frac{F_{seg}}{A_{projected}} \leq \frac{f_y}{\gamma_{M2}}$$

Where: $\gamma_{M2} = 1.25$ (the partial safety factor for the resistance of plates in bearing [38]).

The ideal ratio between the stresses can be calculated as follows:

$$\frac{\sigma_{net}}{\sigma_{contact}} = \frac{\gamma_{M2}}{\gamma_{M1}} = 1.14$$

Hence, for equal utilisation:

$$\frac{\sigma_{net}}{\sigma_{contact}} = \frac{\frac{F_{seg}}{t * (l_{seg} - d_{hole})}}{\frac{F_{seg}}{t * d_{dowel}}} = 1.14$$

Assuming $D_{hole} = 1.15 * D_{dowel}$, to allow for tolerances of the hole, the relationship between the ideal segment length and the diameter of the dowel can be calculated:

$$l_{seg} = 2.03\ d_{dowel}$$

Assuming $d_{dowel} = 200\ mm$ and $h_{dowel} = 250mm$ as starting points for the design. A dowel of this size will lead to a segment length:

$$l_{seg} = 406\ mm$$

5.3 Required horizontal preload

External load per segment is calculated using the line load from Table 1.1.

$$F_{seg} = Q * l_{seg} = 4.42 * 10^6\ N$$

A vertical preload equal to 100% ULS load level is used as a starting point to ensure that sufficient preload is available. The amount of horizontal preload required can be found using the equation (4.4).

$$F_H = \frac{F_P}{\frac{\cos\alpha(1 - \mu * \tan\alpha)}{(\sin\alpha + 2\mu\cos\alpha - \mu^2\sin\alpha)}}$$

For a dowel angle of $\alpha = 5°$ and $\mu = 0.2$

$$F_H = 2.18 * 10^6\ N$$

5.4 Flange verification

Assuming the same thickness as the MP for the lower flange of 150mm. The same thickness is used for the upper flange, but each web is made thicker due to the lateral bending of the tips of the webs, so each web is 120mm thick.

$$t_{LF} = 150mm \quad t_{webs} = 120mm$$

Assuming S355 steel, the stress experienced by the net area of the segment is:

$$\sigma_{net} = \frac{F_{seg}}{A_{net}} = 168.12\ MPa$$

$$P_{contact} = \frac{F_{seg}}{A_{projected}} = 147.42\ MPa$$

Unity checks:

$$UC_{net} = \frac{\sigma_{net}}{\frac{f_y}{\gamma_{M1}}} = 0.5 \qquad UC_{contact} = \frac{P_{contact}}{\frac{f_y}{\gamma_{M2}}} = 0.5$$

The flanges have sufficient resistance.

5.5 Dowel verification

The loading of the dowel can be idealised as a three point bending problem in order to perform resistance verification.

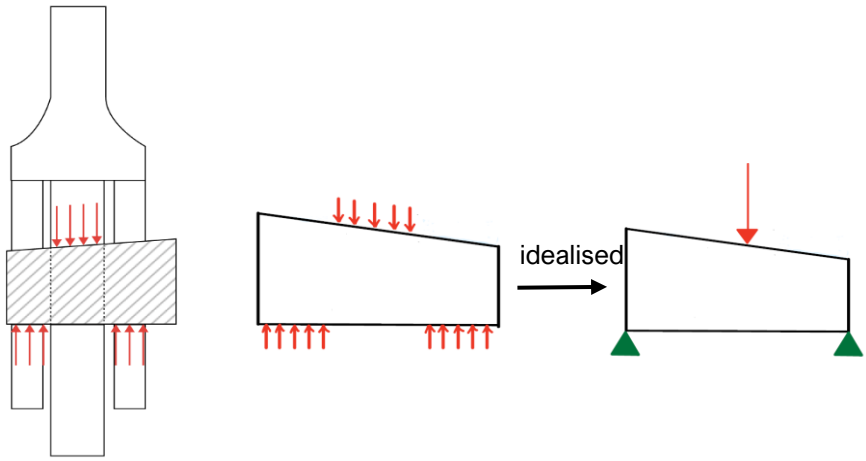

Figure 5.2: Schematic of the dowel as a 3 point bending problem

It is important to note that the dowel has a changing geometry along its length due to the inclined plane. For this calculation, the stresses along the height of the cross section at the mid-section are calculated.

$$L_{dowel} := t_{LF} + 2t_{UF,webs} = 390\ mm$$

$$M_{dowel} = F_{seg}\frac{L_{dowel}}{4} = 4.31 * 10^8\ Nmm$$

Max shear stress within dowel (at centre of symmetric cross section):

$$\sigma_{xm} = \frac{F_{seg} * S_{zz}}{I_{dowel} * b_{dowel}} = 148.45\ N/mm^2$$

Where S_{zz} is the first moment of area at the centre of the dowel.

Bending stress is maximum at extreme fibres of cross section

$$\sigma_b = \frac{M_{dowel} * y}{I_{dowel}} = 322.8\ N/mm^2$$

Where I_{dowel} and y are the second moment of inertia and distance from neutral axis of the dowel respectively.

Unity checks:

$$UC_1 = \frac{\sigma_{xm}}{\frac{f_y}{\sqrt{3}}} = 0.72 \qquad UC_2 = \frac{\sigma_b}{f_y} = 0.91$$

The dowel has sufficient resistance.

5.6 Details and dimensions of preliminary design

Based on the analytical calculations, the preliminary design of the connection is created, the dimensions of which are shown in Table 5.1 below.

Table 5.1: Preliminary design of connection

Dowel diameter	200	mm
Dowel height	250	mm
Thickness of flange	150	mm
Segment length	406	mm
No of dowels	93	-

5.6.1 3D Model

A 3D model of the connection is created using the CAD software SOLIDEDGE and shown in Figure 5.3.

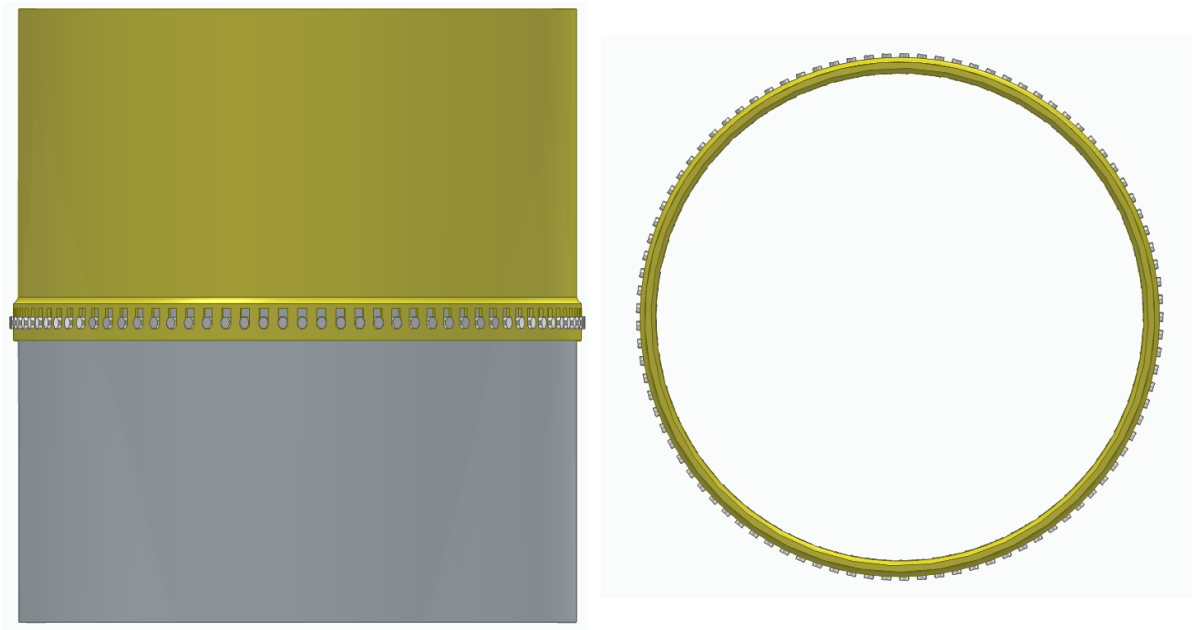

Figure 5.3: 3D model of the connection, side view (left) and top view (right)

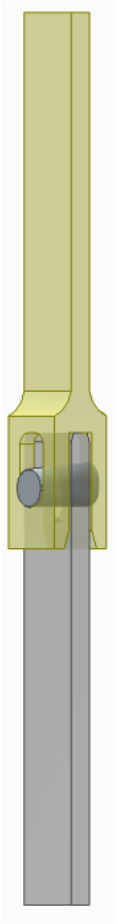

Figure 5.4: A single segment of the connection

A segment of the connection is then extracted as shown in Figure 5.4. The segment length is 406mm based on the calculations in section 5.2. The dimensions of the components of the connection are shown below.

5.6.2 Lower Flange

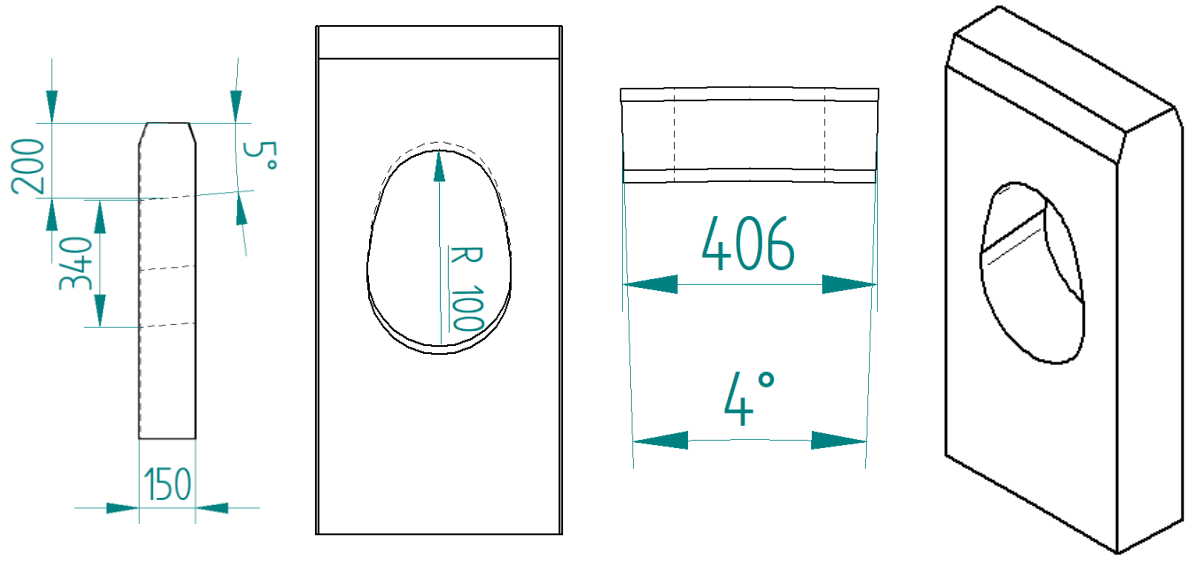

Side view Front view Top view Isometric view

Figure 5.5: Dimensions of the LF (all dimensions in mm)

5.6.3 Upper flange

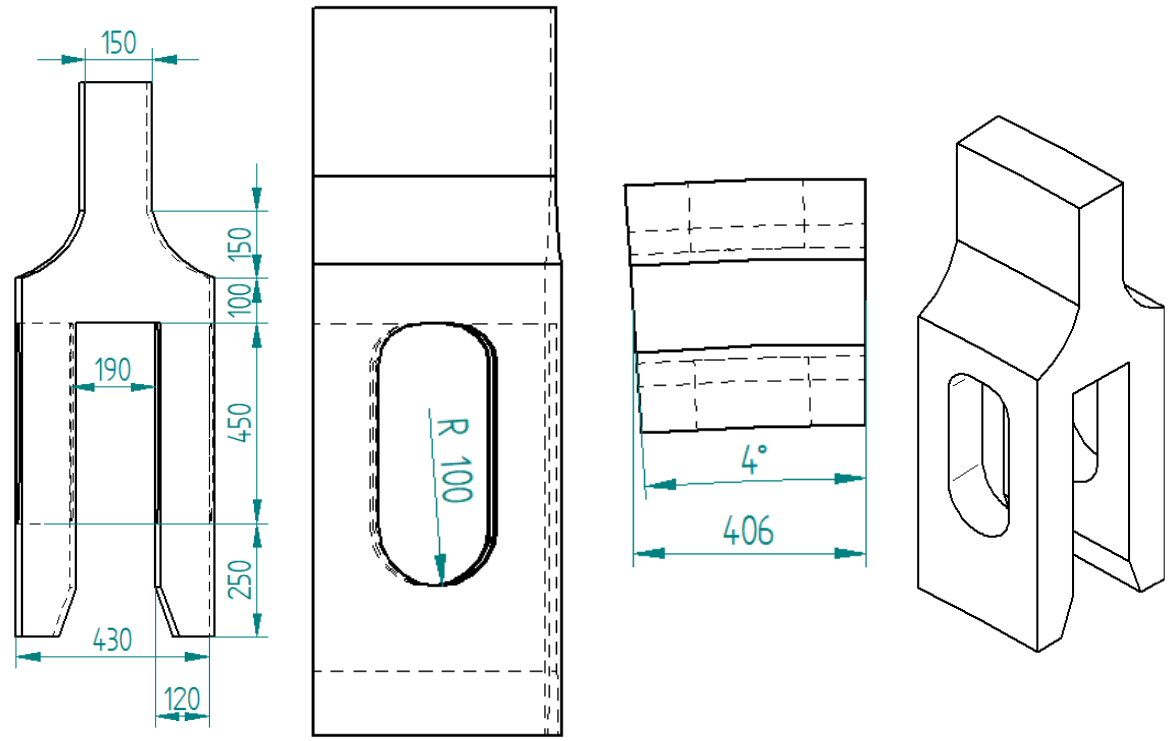

Side view Front view Top view Isometric view

Figure 5.6: Dimensions of the UF (all dimensions in mm)

5.6.4 Dowel

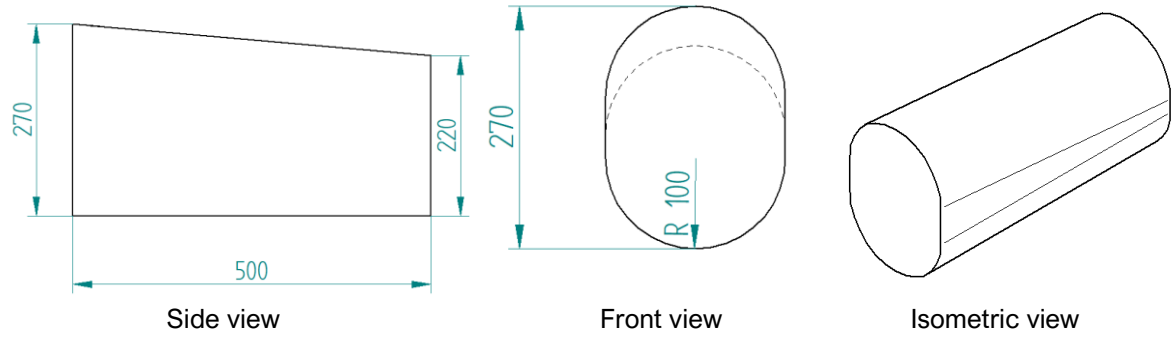

Figure 5.7: Dimensions of the dowel (all dimensions in mm)

6 Description of Numerical Model

In this chapter, details of the FE model used for analysis is introduced. The purpose of the numerical study is to understand the structural behaviour of the connection in greater depth compared to analytical models. Numerical modelling allows for the analysis of more complex structural behaviour involving complex shapes. A half segment is analysed to reduce computational demands by taking advantage of the symmetry of the connection. Figure 6.1 presents the geometry of the half segment model. The components are positioned such that the lower dowel is in contact with the holes of each flange. The height of the model, excluding flanges, amounts to 2m.

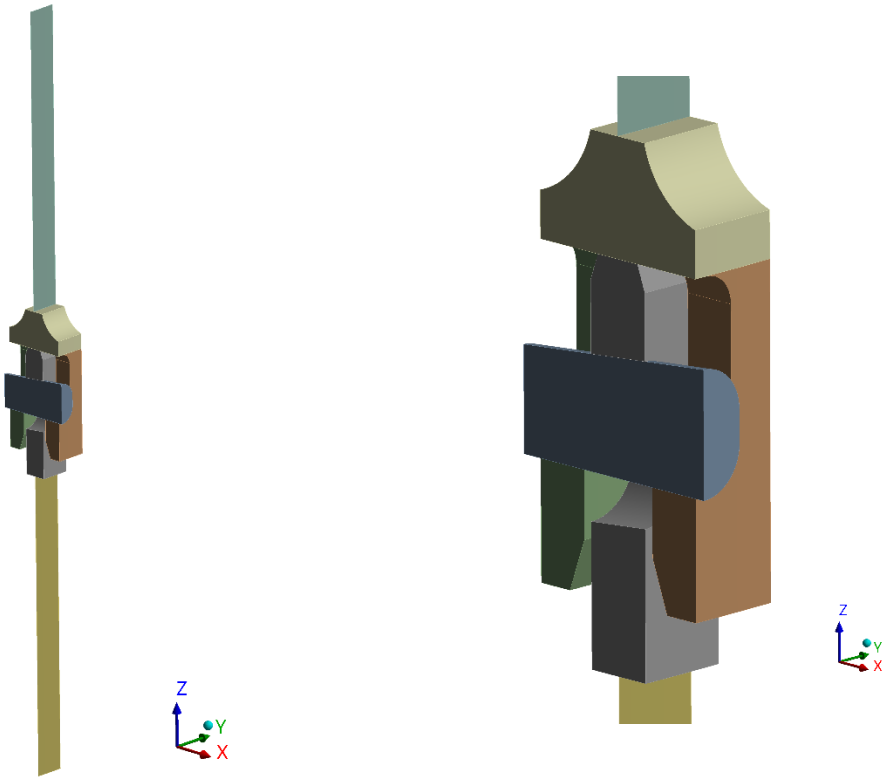

Figure 6.1: Geometry of FE model, full model (left) and the connection in focus (right)

6.1 Software and solver details

ANSYS is the chosen FEA software for this study. An implicit static analysis is used as the problem as a static state is assumed. There are two solver types in ANSYS: direct and iterative. For non-linear analyses involving contact problems the direct solver is usually preferred and is therefore the solver used in this analysis [39].

6.2 Mesh

Figure 6.2 presents a general overview of the mesh of the half segment model.

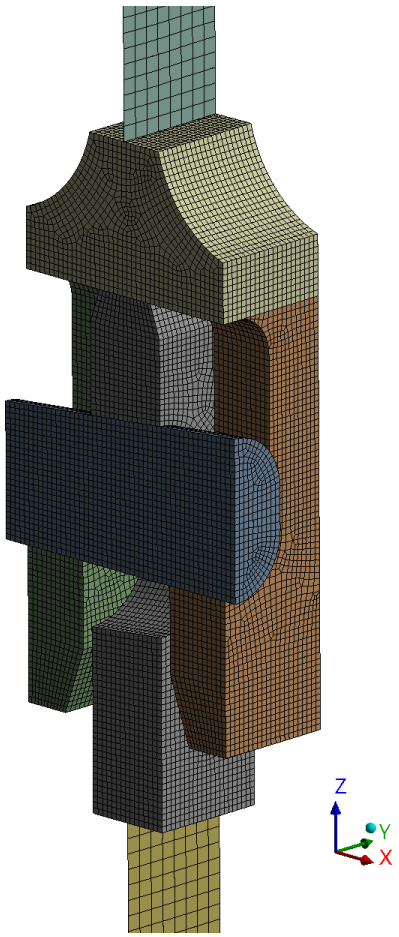

Figure 6.2: Meshed half segment model

Linear hexahedral elements (Solid185) are used for the flanges and the dowel, while shell elements (Shell 181) are used for the tower sections above and below the connection. SOLID185 Structural Solid is suitable for modelling general 3-D solid structures. It is defined by eight nodes having three degrees of freedom at each node: translations in the nodal x, y, and z directions, using linear interpolation between the nodes. SHELL181 is suitable for analysing thin to moderately-thick shell structures. It is a four-node element with six degrees of freedom at each node: translations in the x, y, and z directions, and rotations about the x, y, and z-axes. A mesh size of 10mm is used for the solid elements and a mesh size of 20mm is used for the shell elements. A mesh sensitivity study is performed and the results are shown in Appendix B: Mesh sensitivity.

6.3 Contact

6.3.1 Contact formulations

The contact in ANSYS is based on defining a contact body and a target body. Target part can penetrate the contact body if it does not contact a detection point on the contact body. To avoid this, it is recommended that the contact part is the most flexible part and if the surfaces are curved then the most convex surface should be the contact part [39]. The Augmented Lagrange method is the default choice

in ANSYS for frictional contact surface formulations. It is preferred over traditional penalty-based methods, which involve defining a penalty stiffness at contact and penalizing penetrating nodes. Another option, the normalized Lagrange method, addresses penetration by solving for contact pressure but is computationally intensive and can lead to over-constraints. Augmented Lagrange effectively handles complex contact problems, introducing minimal and controllable penetration effects, rendering them negligible [40].

6.3.2 Contact detection

The detection method determines which nodes or points on the contact should be used in the contact formulation. These are then constrained against the penetration of the target surface [39]. Nodal detection method are used for the surface-surface contacts as it provides good results with minimal contact pressure spikes at nodes [40].

6.3.3 Contact elements

CONTA174 element is used to represent contact and sliding between 3-D target surfaces and a deformable surface defined by this element. The target surface is defined by the 3-D target element type, TARGE170.

6.3.4 Contact surfaces

For contact elements CONTA174 coulomb friction is used in ANSYS. It defines the point of sliding with an equivalent shear stress, τ, that is dependent on the coefficient of friction and the contact pressure. When this shear stress is reached, the surfaces will start sliding relative to each other. As default it uses a constant value of the coefficient of friction [39]. Four contact surfaces are identified between the following components. The type of contact and friction coefficient are presented in Table 6.1.

Table 6.1: Contact definitions in the FE model

Contact	Target	Type	μ
Upper Flange	Lower Flange	Frictional	0.2
Dowel	Lower Flange	Frictional	0.2
Dowel	Upper flange outer web	Frictional	0.2
Dowel	Upper flange inner web	Frictional	0.2

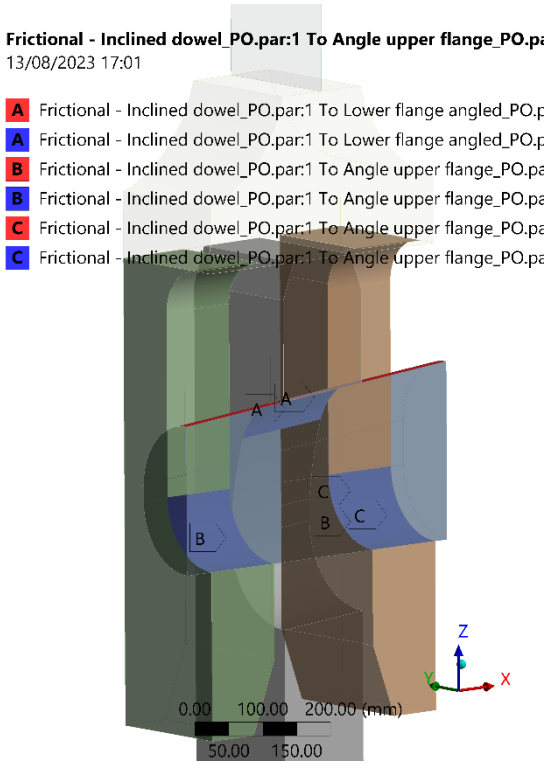

Figure 6.3: Contact regions in FE model

6.4 Material Model

As discussed in section 3.3, the same material will be used for both flanges and the dowel. A Non linear material with yield reduction with thickness according to EN 10025-3:2019 is used [41]. The thicknesses and reduced yield stress is shown in Table 6.2: Yield strength of the components of the connection

Table 6.2: Yield strength of the components of the connection

Component	Thickness	Reduced Yield strength [MPa]
Upper flange	430	275
Lower flange	150	295
Dowel	200	285

The following nonlinear model is developed by using the relation between true stress and strain acc. to DNV RP C208 [42]. The following material properties are used in all material definitions:

Modulus of Elasticity (E): 210.000 N/mm^2

Poisson's ratio (ν): 0.3

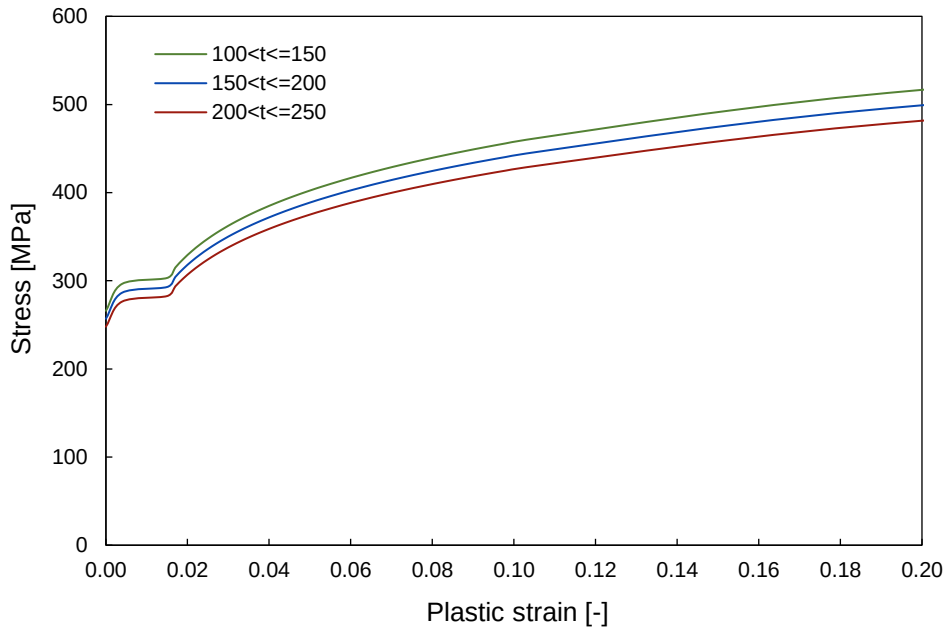

Figure 6.4: S355NL stress-strain curves according to EN 10025-3:2019

It is assumed that there are no welds in the connection and therefore the upper is made from one plate. The thicknesses of the components are above standard thicknesses, and hence the minimum yield strength is assumed.

6.5 Boundary Conditions

Symmetric boundary conditions are used in the FE analysis of pressure vessels and cylinders to reduce the size of the model [43]. Displacement of the faces and edges at the cut interfaces in the normal direction are restrained as shown in Figure 6.5. This allows for the hoop and radial stiffness of the overall tubular to be captured within the segment model.

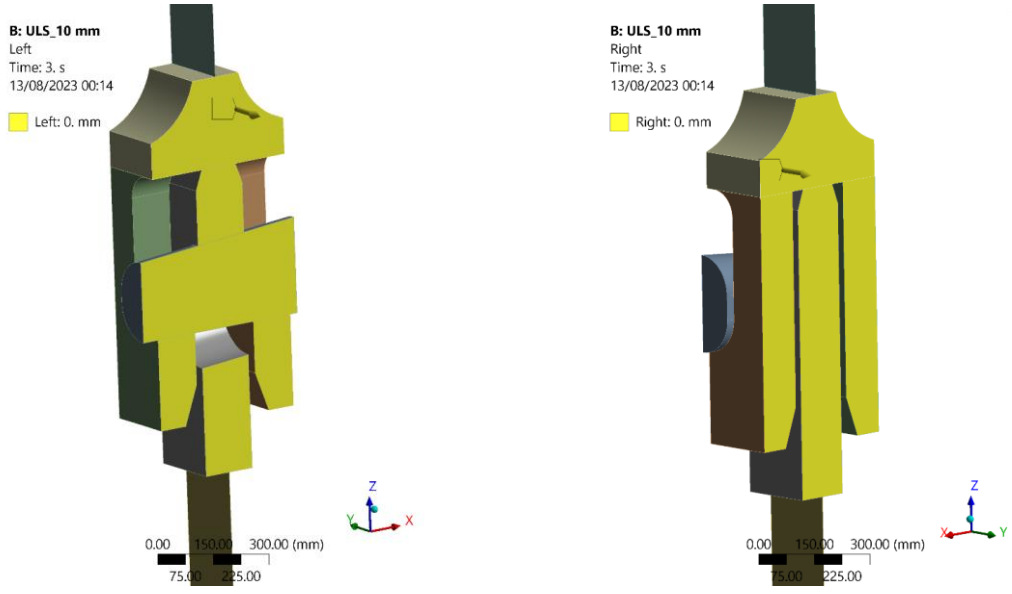

Figure 6.5: Boundary conditions at the segment interfaces

The effect of these boundary conditions and its ability in simulating the ring stiffness of the tubular is presented the boundary condition verification in Appendix C: Boundary Condition Verification: C.1 Symmetric boundary condition verification. Aside from this, the model is also fixed at the bottom to prevent rigid body motion.

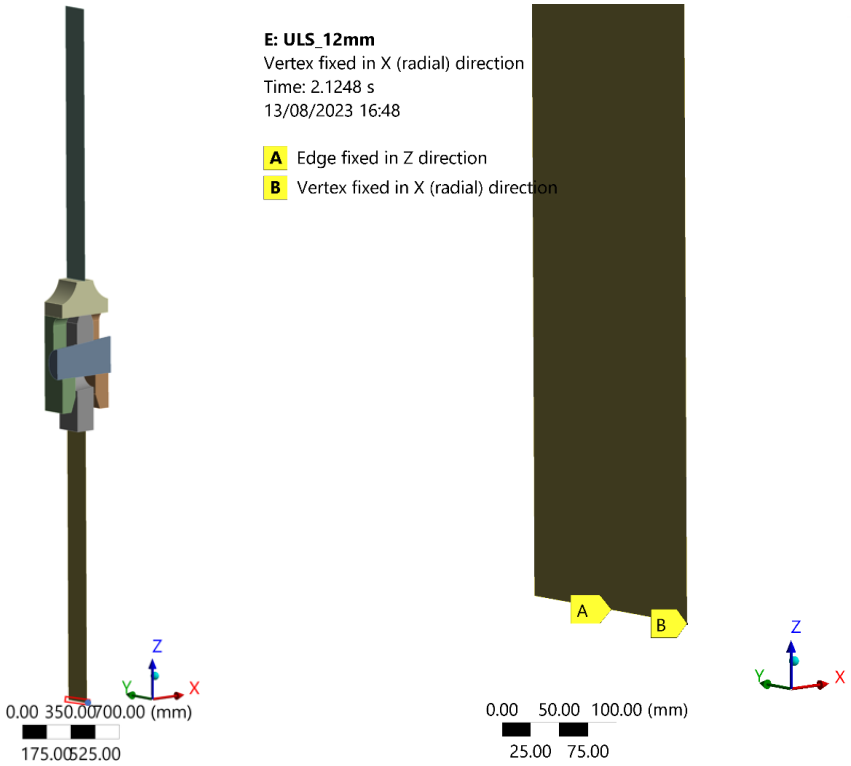

Figure 6.6: Boundary conditions at the bottom of the segment

This boundary condition is purely to ensure that there is no rigid body motion in the model and should not provide additional radial or hoop stresses, which can lead to inaccurate results in the analysis. To ensure this, the edge is placed 2m below the connection level so that its effect on the structure is negligible. This is verified through a sensitivity analysis in Appendix C.2 Boundary condition sensitivity.

6.6 Loads

The loads applied onto the model are done in load steps. In the first loadstep a horizontal load is applied onto the dowel as shown in Figure 6.7. This is followed by the removal of this load in the subsequent loadstep and then an external load (either tension or compression) is applied onto the top of the model.

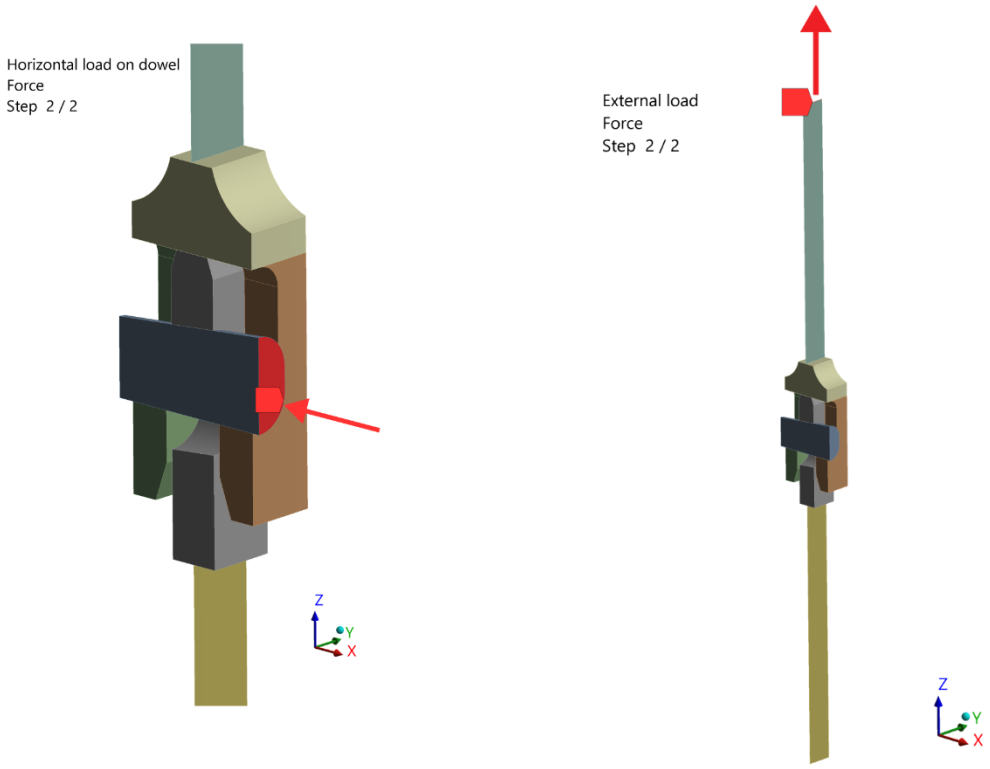

(a) (b)

Figure 6.7: Application of (a) horizontal load and (b) external load

7 Numerical Analysis

The results from the FE analysis of the connection is presented in this chapter. The structural behaviour during installation and under external loading is observed. Aside from this, a sensitivity analysis on the friction coefficient and preload level is performed.

7.1 Installation

7.1.1 Preload development

The relationship between the vertical preload between the flanges, F_p and the horizontal preload on the dowel, F_H is shown in Figure 7.1.

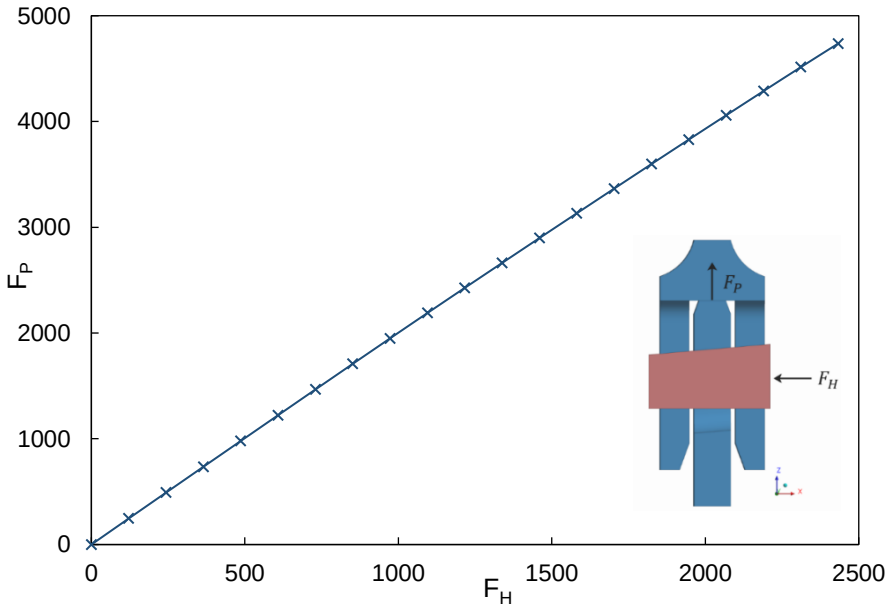

Figure 7.1: Vertical preload vs horizontal preload on dowel

The vertical preload is calculated at the contact force between the upper flange and lower. The total vertical force across the contact elements as the analysis progresses is measured. It is seen that the vertical preload increases linearly with the horizontal load applied on the dowel. The horizontal preload is magnified by a factor of 1.95. This shows a 4% difference between FE and analytical model that predicted a mechanical advantage of 2.03. This difference is very low and can be attributed to the energy lost in plasticity during installation and through the bending of the flanges and dowel which not predicted in the analytical calculations.

7.1.2 Radial deformation of flanges

The upper and lower flanges deforms radially as the dowel is installed. The deformation of the flanges with increasing horizontal load is shown in Figure 7.2 and Figure 7.3.

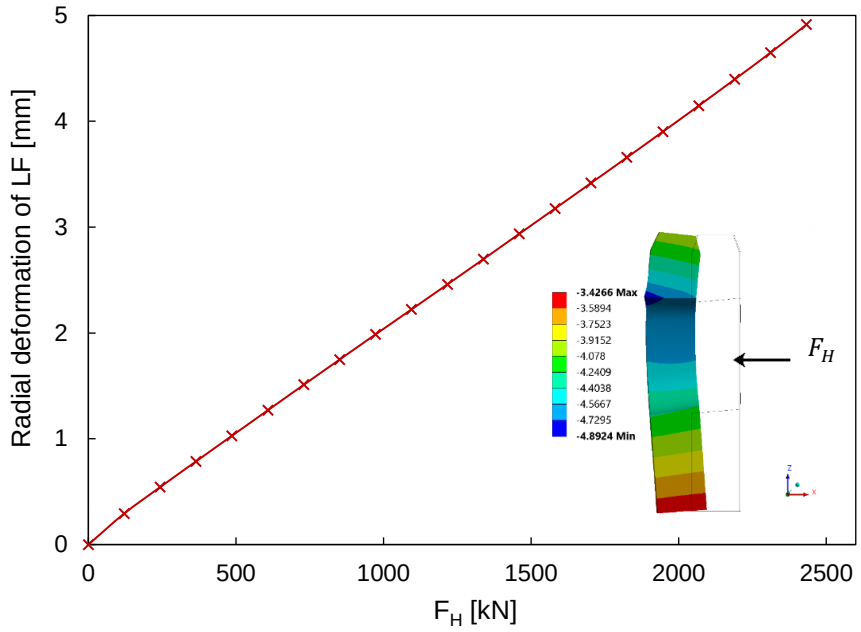

Figure 7.2: Radial deformation of lower flange [contour plot is scaled 20x]

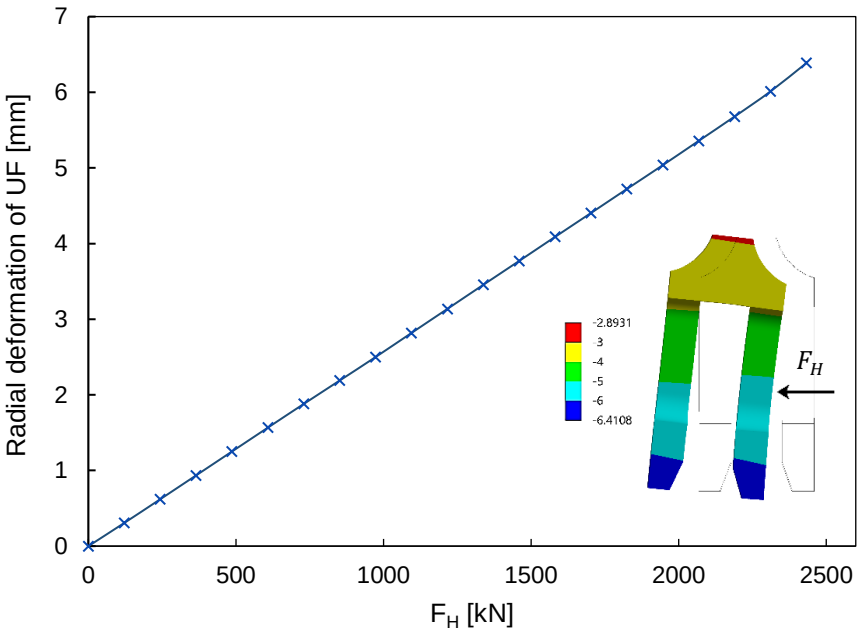

Figure 7.3: Radial deformation of upper flange [contour plot is scaled 20x]

The absolute maximum deformation on either body is measured in the plots. The radial deformation increases linearly with increasing horizontal load. The linearity of the deformation indicates that a significant proportion of the deformation of the flanges is elastic. The clearance between the flanges is 20mm, which is sufficient to ensure that the flanges do not collide with each other during installation.

7.1.3 Stress and strain

To further observe the behaviour of the connection during the installation process, the stresses and strains within the connection are analysed below.

7.1.3.1 Maximum principal stress

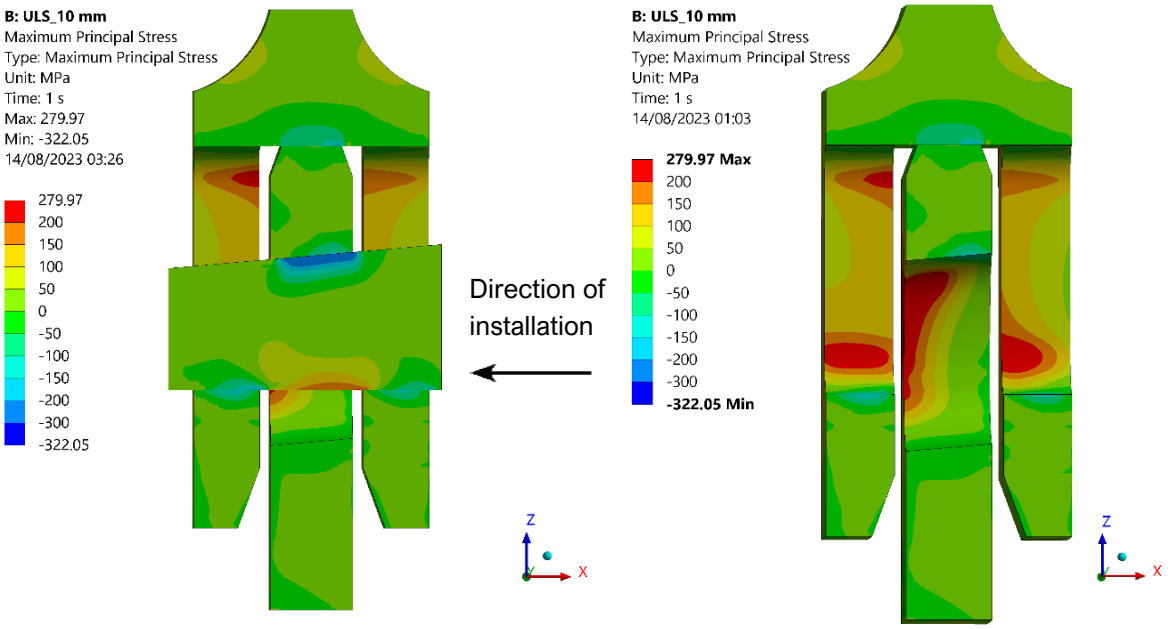

(a) With dowel in position (b) Without dowel

Figure 7.4: Maximum principal stress within the connection during installation

The bending of the dowel is evident through the region of compression in the top half and tension in the bottom half of the dowel. This is further investigated below. The plot on the right also indicate bending in the UF webs. This is expected as the webs will bend as the dowel deforms them radially.

7.1.3.2 Directional stress

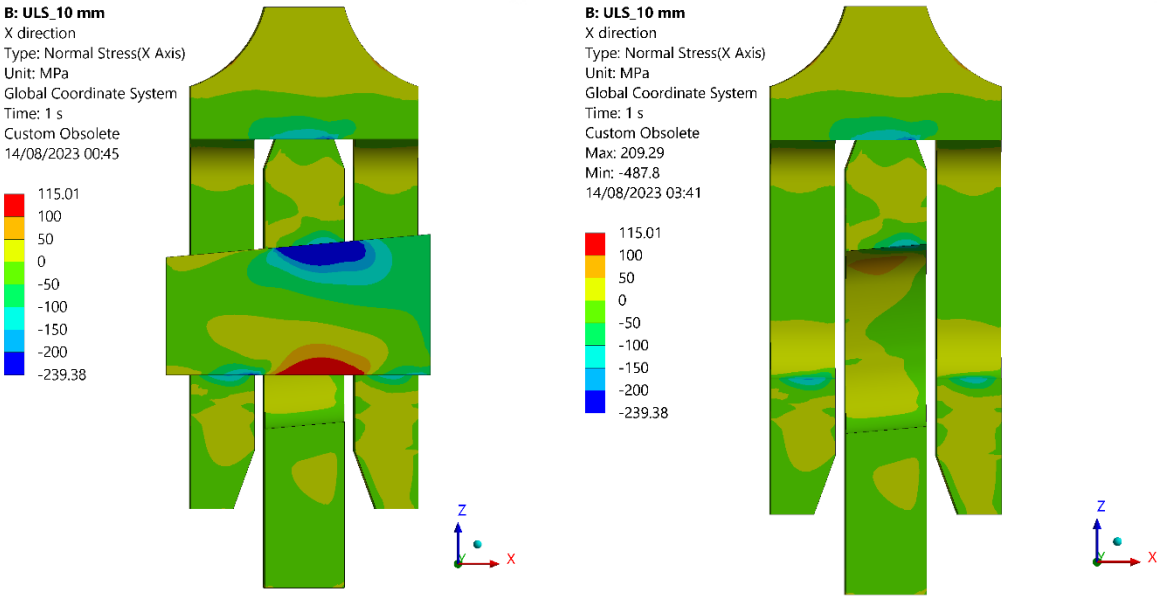

Figure 7.5: Normal stress in X direction during installation

Figure 7.5 shows the bending of the dowel about the y axis when its installed. There is a region of compression on the top half of the dowel and tension on the bottom half. This was expected based on assumption in section 5.5 where the loading of the dowel is similar to a 3-point bending beam. The bending stress shown in FE is within the same order of magnitude as what was predicted in the analytical calculations. The difference is due to the analytical calculations not taking into account the changing geometry of the dowel along its length, and hence changing bending resistance.

7.1.3.3 Shear stress

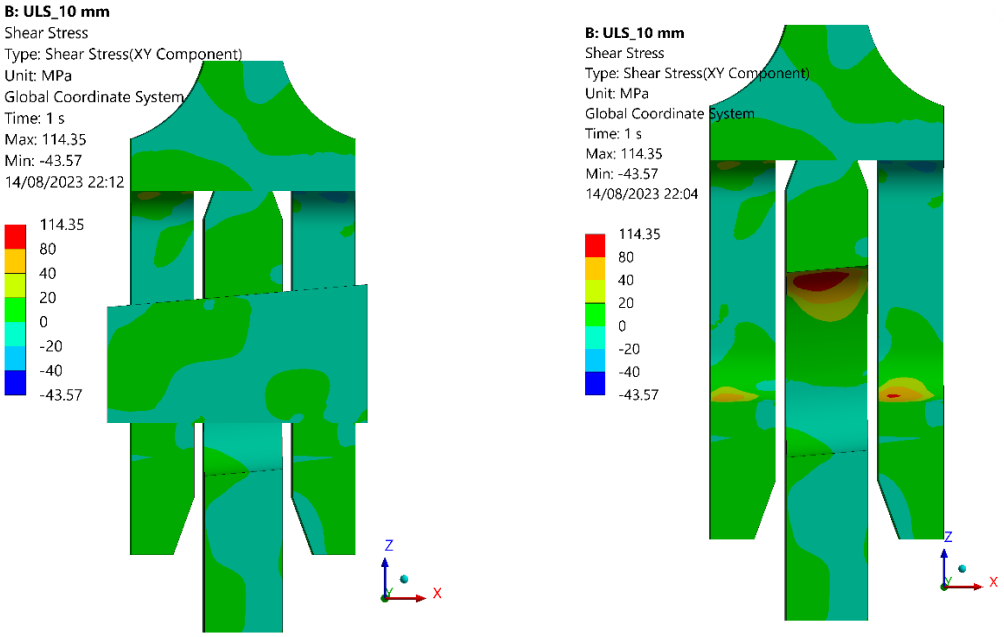

Figure 7.6: Shear stress in XY plane during installation

The plot on the left shows a region of high shear stress at the locations of dowel to flange contact. This is likely due to the frictional stress between the dowel and flanges that builds up during the installation.

7.1.3.4 Development of plasticity

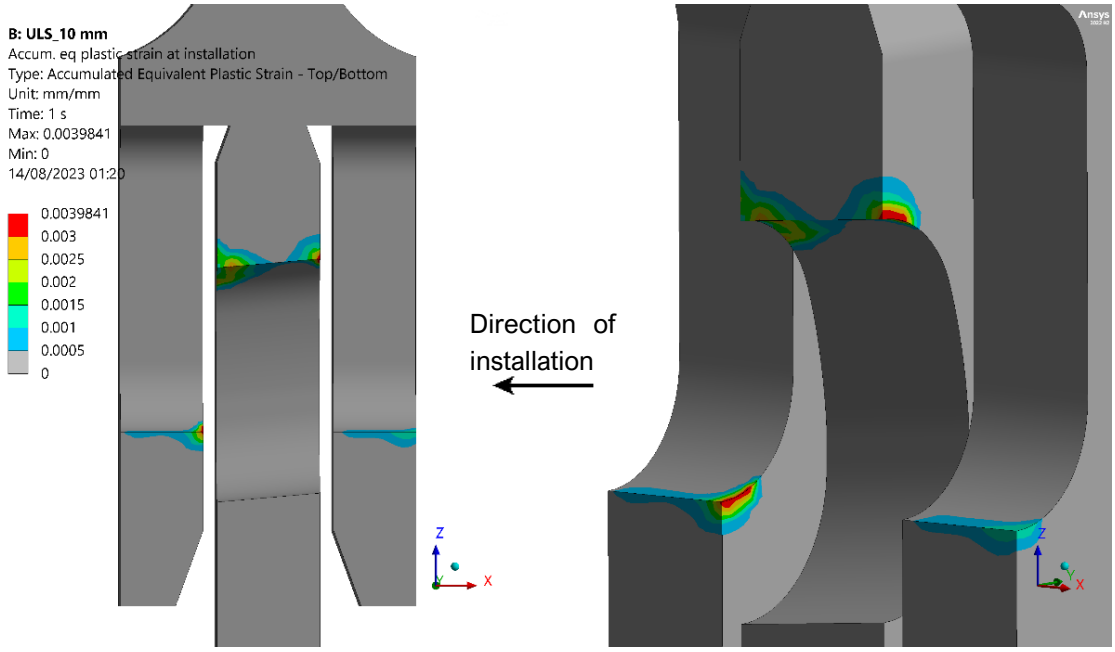

Figure 7.7: Accumulated equivalent plastic strain

Figure 7.7 shows the distribution of equivalent (von Mises) plastic strain within the structure after the installation. The areas where plastic strain develops are concentrated in the regions of contact between the dowel and flange. When the dowel is installed, the flanges bend with the highest stresses occurring at the edges of the holes. This along with the dowel itself that bends onto the flanges explains the plasticity that develops in these regions. The magnitude (<0.5%) and extent of plastic strain remains low and therefore the connection can withstand the installation force.

7.1.4 Contact stresses

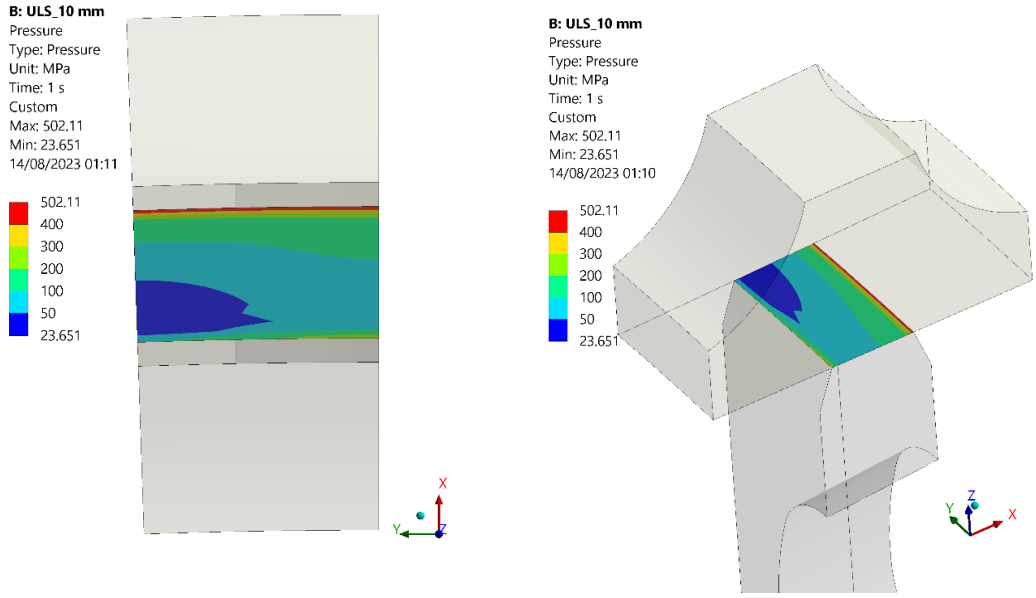

Figure 7.8: Contact stress between the LF and UF

Figure 7.8 shows a non-uniform pattern of the contact stress between the two flanges. The peak stress occurs at the edge of the contact area, which is a consequence of the bending of the crown. The stress is also distributed along the y-axis with stresses the highest above the dowel.

7.1.5 Discussion of the results from installation process

The connection shows an adequate resistance against the installation process. The clearance between the flanges is 20mm, which is sufficient to ensure that the flanges do not collide with each other during installation. Stresses in the structure are below the yield limit and there is no excessive plasticity in the connection. The FE model also shows similar correlations to the expected behaviour from the analytical models derived.

7.2 Relaxation

7.2.1 Introduction

To verify the self locking nature of the connection, an analysis with 2 load steps is performed as shown in Figure 7.9. In load step 1, the horizontal load, F_H is applied onto the dowel creating the vertical preload, F_p. Over load step 2, F_H is reduced to 0 to simulate the removal of the horizontal actuation force. The value of F_P across these two load steps are plotted in Figure 7.9.

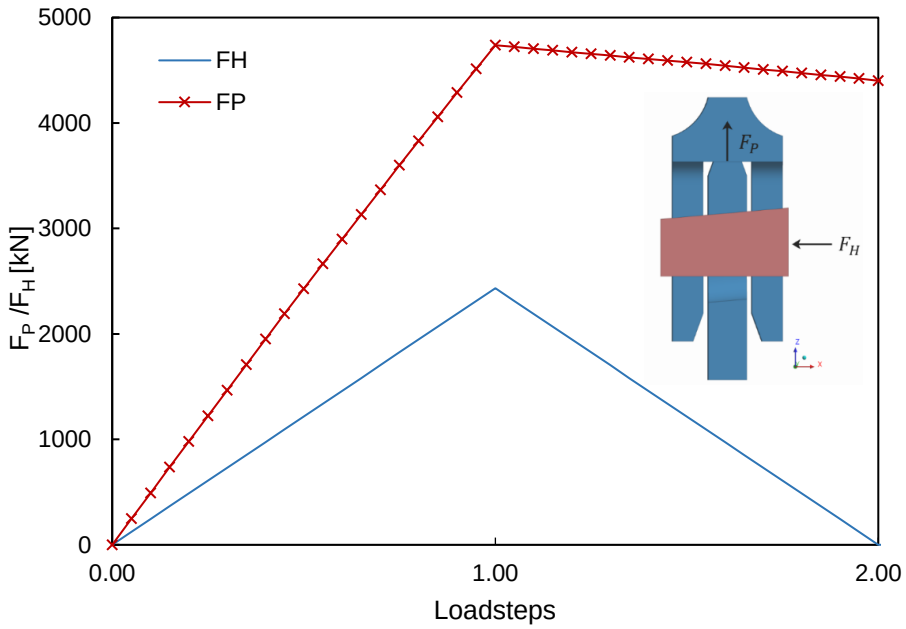

Figure 7.9: Load application on model

Across the second load step, after the removal of the installation load, it is apparent that the connection experiences a loss of original preload by 7%.

7.2.2 Sliding of dowel

It is important to verify that the dowel is self-locking as the sliding out of the dowel can cause a loss of preload between the flanges. To investigate this, the sliding of the dowel against the surfaces of the

flanges is analysed and presented in Figure 7.10. This is measured in ANSYS by calculating the relative displacement between two contact surfaces.

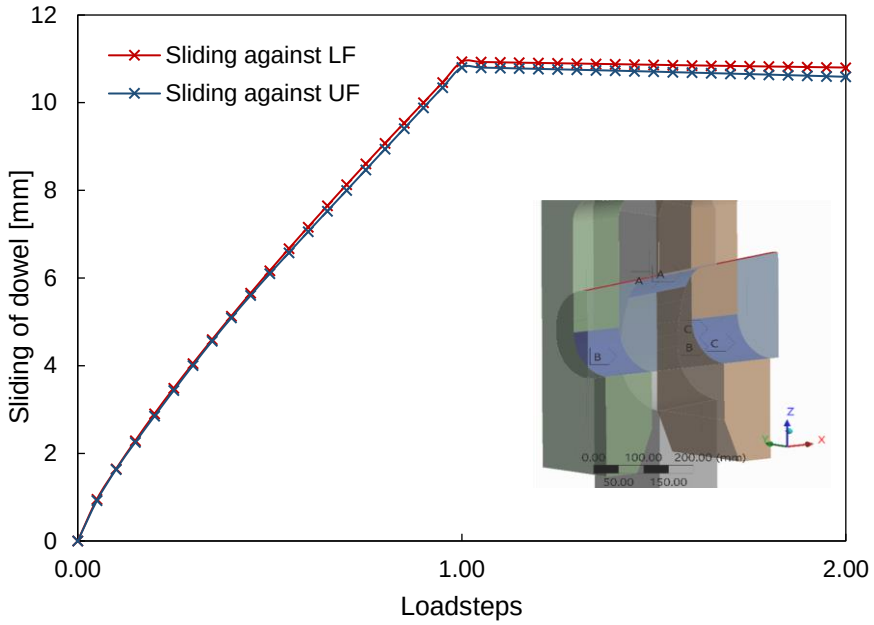

Figure 7.10: Sliding of dowel

Table 7.1: Sliding out distance of dowel in second loadstep

	Against LF	**Against UF**
Sliding distance [mm]	0.1	0.2

The data shows that the dowel does slide out against each surface however the magnitude does remain low. The expected preload loss from the sliding of the dowel is 2% as shown in Table 7.2. This suggests that the sliding of the dowel is not the sole contributor towards the overall relaxation.

Table 7.2: Expected preload loss from the sliding out of the dowel

Stroke (vertical preload per mm)	449	kN
Sliding distance	0.22	mm
Expected preload loss from sliding of dowel	97.40 (2%)	kN
Actual preload loss	338 (7%)	kN

7.2.3 Elastic deformation of flanges

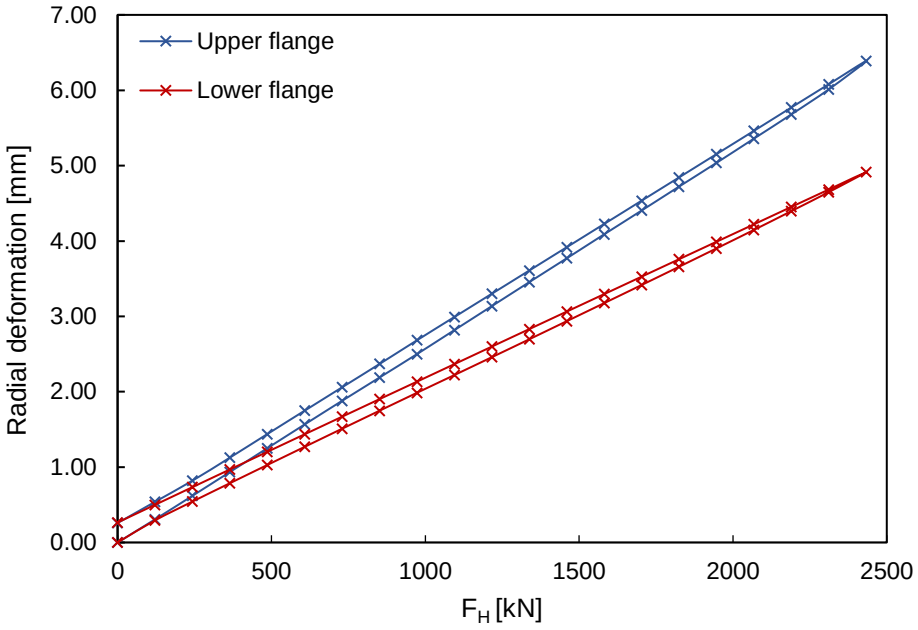

Figure 7.11: The radial deformation of the upper and lower flanges

The radial deformation of the flanges are studied and presented in Figure 7.11. It is seen that although there is a small level of permanent deformation, the deformation of the flanges is mostly elastic, causing the flanges to deform back to its original position. This is also evident from the deformation plots shown

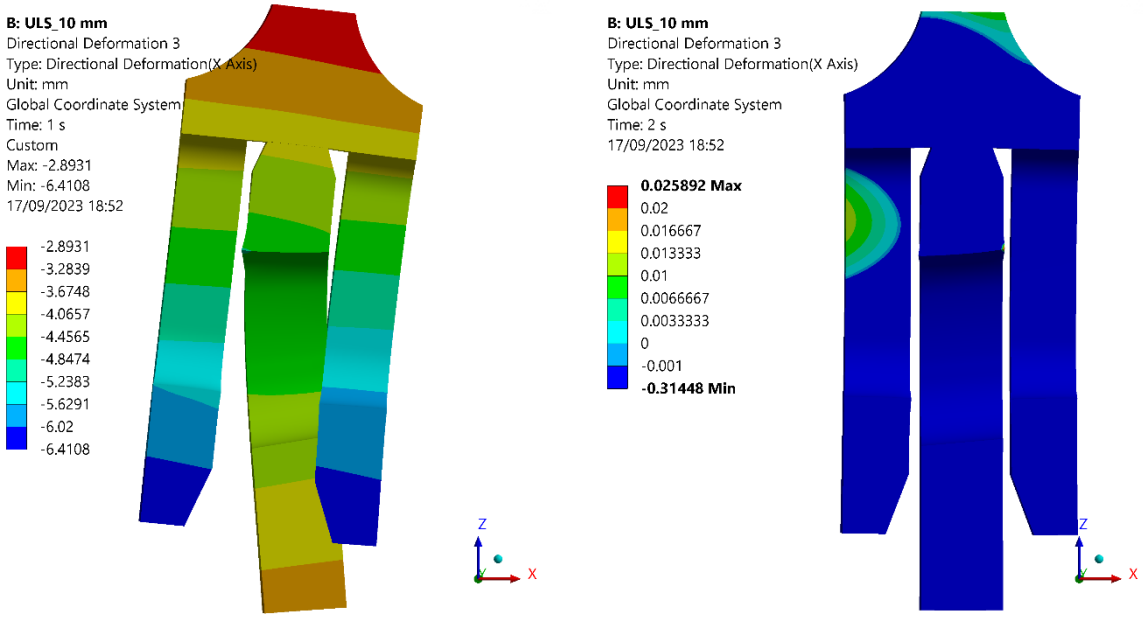

(a) Loadstep 1 b) Loadstep 2

Figure 7.12: Deformation of the flanges over the two loadsteps (scaled by 30x)

7.2.4 Discussion of the relaxation of the connection

A loss in preload can be due to many factors and is a common phenomenon in other connections that relies on the pretensioning or preloading of elements such as conventional bolted connections [23]. Preload loss can occur through relaxation right after pretensioning and a sustained loss over the duration of usage. In this case an immediate relaxation is observed after the dowel has been installed. The elastic energy stored within the flanges during installation causes them to return to their original position once the external load is removed. This causes a reduction in the contact stress between the flanges which was highest at the point of installation. As the magnitude of the relaxation remains low it is assumed to be an acceptable level. Moreover , the relaxation can be accounted for during preloading stage to ensure that residual preload is sufficient to withstand the ULS loads.

7.3 Connection under external load

7.3.1 Load sharing

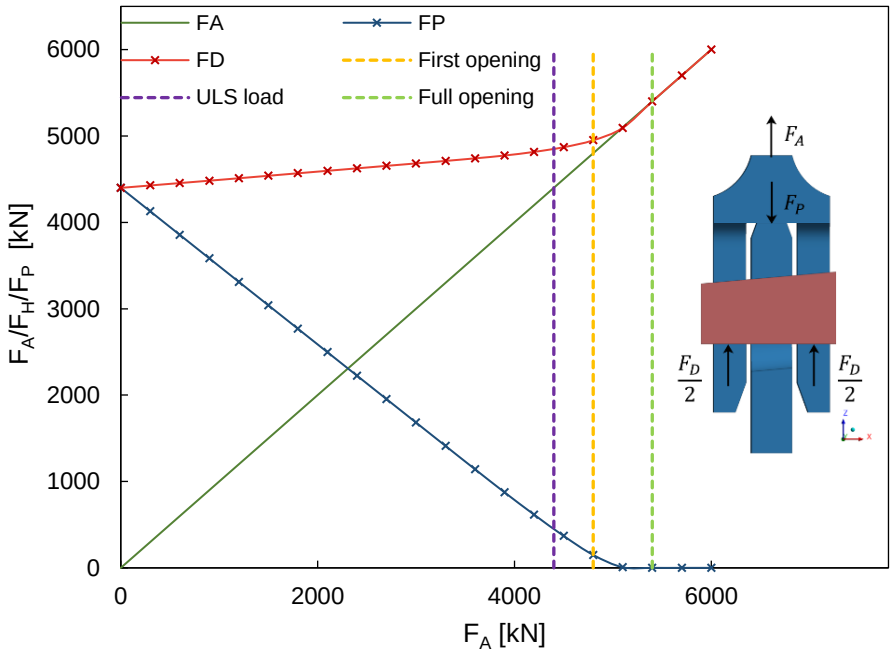

Figure 7.13: Load sharing in connection under external loading

The load sharing through the two load paths in the connection can be observed in Figure 7.13. The plot shows that when the external load is applied, the primary load path is through the reduction of the preload between the flanges. There is a linear reduction in the preload, F_P between the two flanges when the external load, F_A is applied. The dowel only experiences a small proportion of the load, indicated by the shallow and constant slope of the force in the dowel, F_D. When the applied load exceeds the level of preload, the dowel takes all of the applied load. This can be seen in the graph where the slope of the force in the dowel increases steeply and matches the external load applied.

7.3.2 Gap opening

The opening of the connection can be inspected by measuring the gap between the upper flange and lower flange. This is measured in ANSYS by evaluating the distance between contact surfaces. The

results for the development of the gap between the upper flange and lower flange are shown in

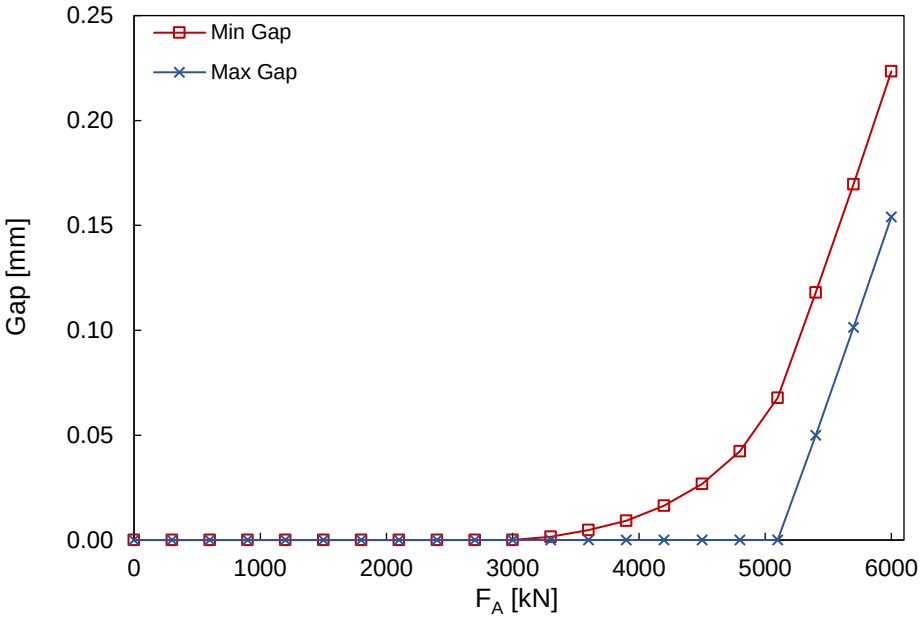

Figure **7.14**.

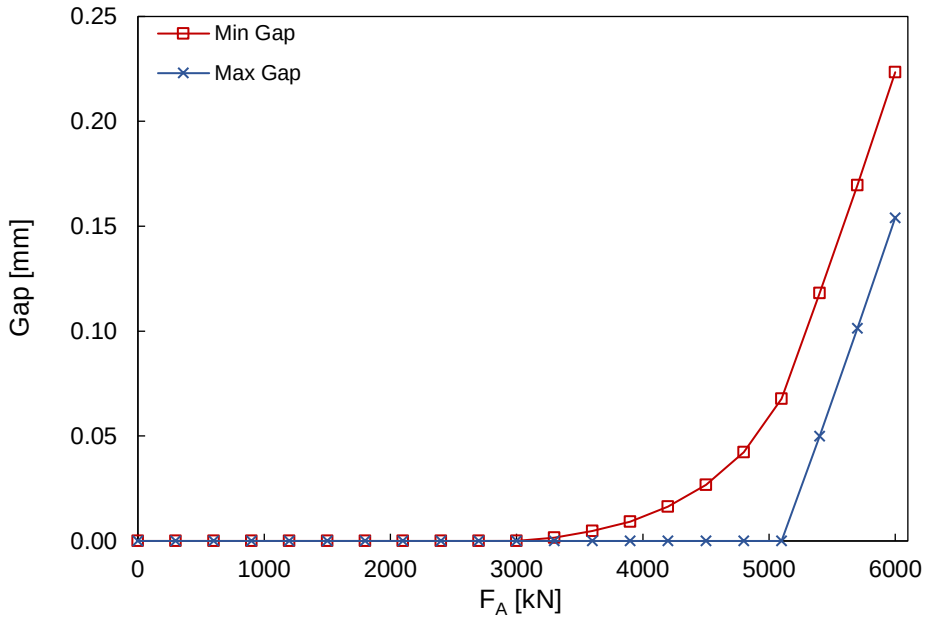

Figure 7.14: Minimum and Maximum gap in the connection vs applied external load

The connection is assumed to have opened after the gap has exceeded 0.05mm. Based on this the loads at which the connections open in are shown in Table 7.3

Table 7.3: External load at which the connection opens

	F_A [kN]
First opening	4800
Fully open	5400

The results show that the connection does not fully open immediately, instead, the connection partially opens first, before fully opening. This can also be observed in the contour plot of the gap shown in Figure 7.15.

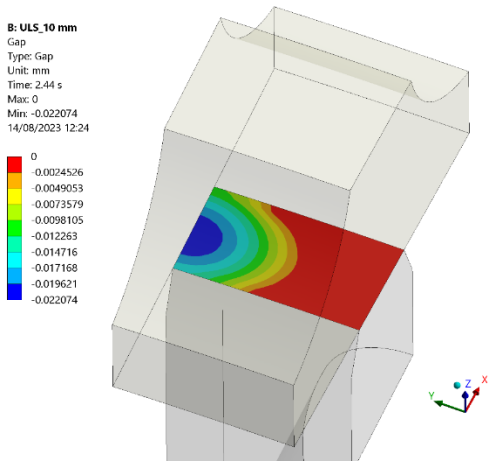

Figure 7.15: Contour plot of the gap between the two flanges

The connection first opens at the ends of the segment away from the dowel. This coincides with the region with the lower contact stress due to the vertical preload between the flanges, previously observed in Figure 7.8. The connection only opens at a load higher than the ULS external load.

7.3.3 ULS loading

7.3.3.1 ULS tension

The maximum principal stress and von-Mises stress under the external tensile (+ULS) load is shown below.

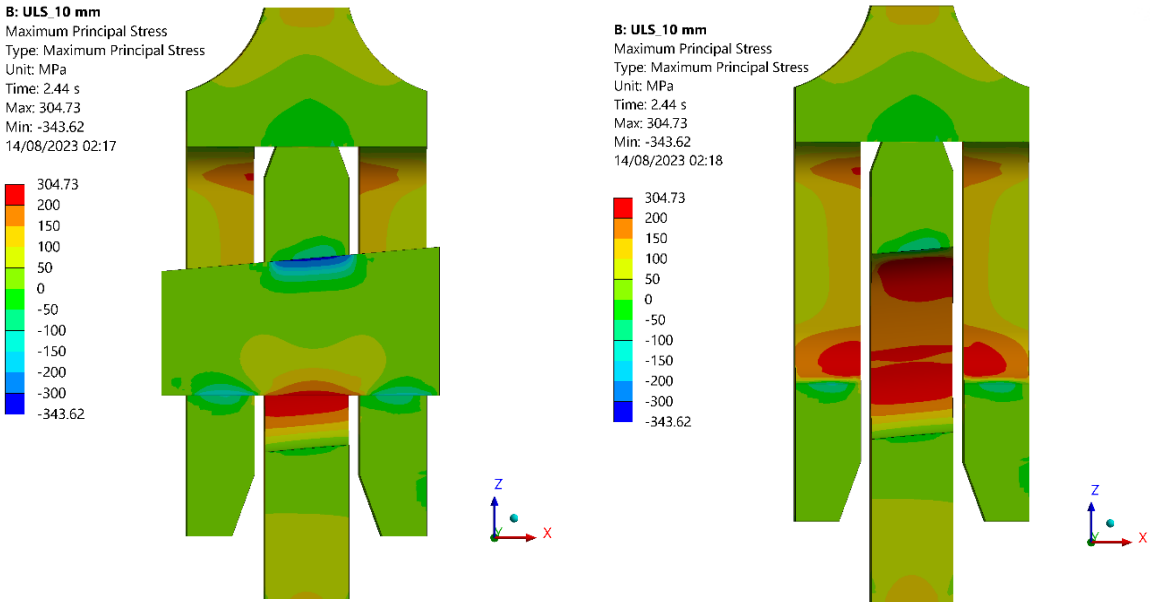

Figure 7.16: Maximum principal stress at +ULS

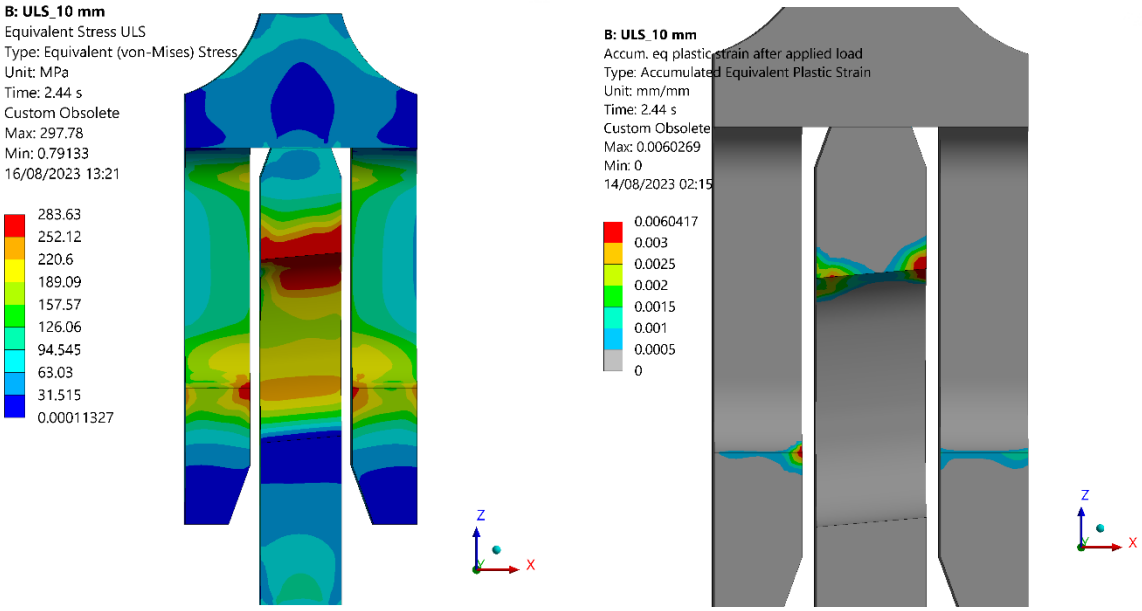

(a) (b)

Figure 7.17: (a) von-Mises stress and (b) plastic strain distribution at +ULS

Figure 7.16 shows that the dowel is experiencing bending. In comparison to the stress plot in Figure 7.4, the increase in bending of the dowel is minimal compared to the installation period. This is because the dowel does not take the full load yet, and the external load is being transferred through the primary load path. The von-Mises stress in Figure 7.17 indicates that regions of high stress are predominantly situated at the contact surfaces between the dowel and flanges. It is observed that the magnitude (<0.6%) and extent of plastic strain remains low and therefore the connection can withstand the loading. There has also not been significant increase in plastic strain around the connection after the installation load.

7.3.3.2 ULS compression

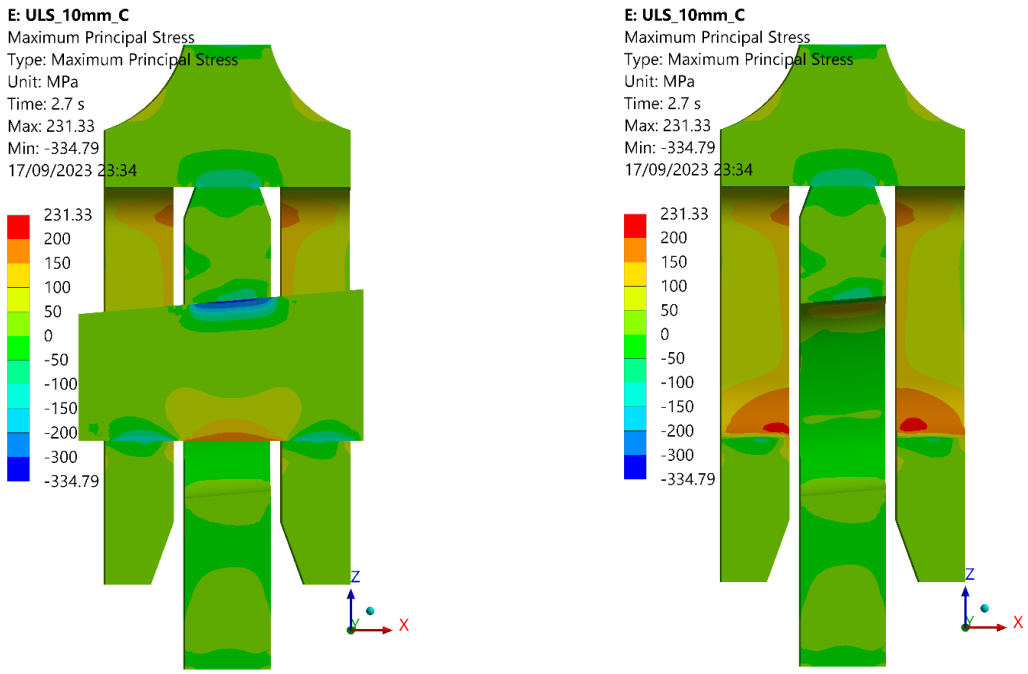

Figure 7.18: Maximum principal stress in the connection at -ULS load

Comparing to the results under +ULS load in Figure 7.16 the flanges are in a lower stress state under the -ULS load. This is because the compression load is transferred directly through the flanges, increasing the interface preload without the dowel experiencing the external load.

7.3.4 Failure of the connection

In order to investigate the failure of the connection, the vertical deformation of the flanges under increasing external load is shown in the figure below. The vertical deformation of the critical location (the node that experiences the greatest vertical deformation) is measured with increasing external tension loading. The location that experiences the greatest vertical deformation is located in the hole of the LF.

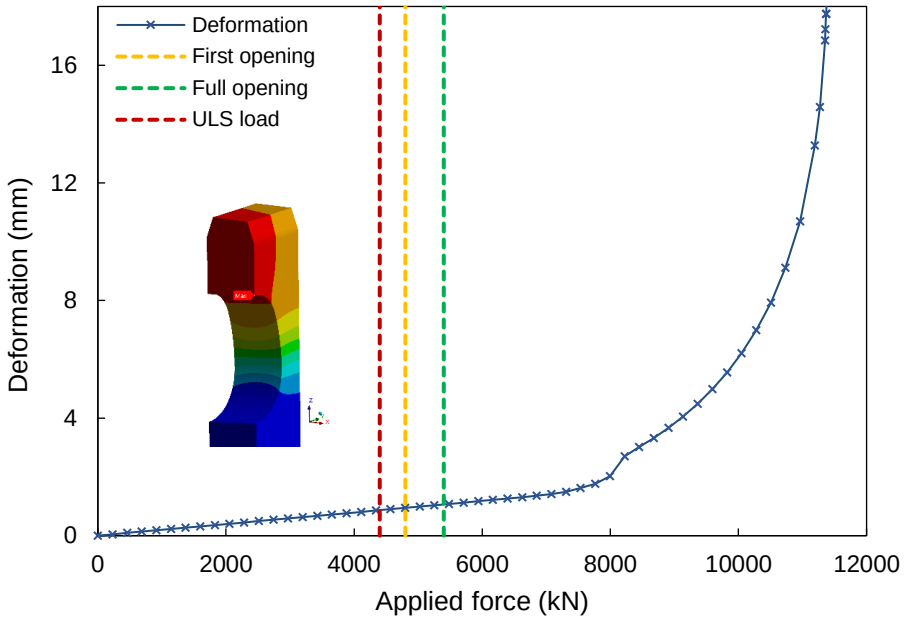

Figure 7.19: External load vs Deformation plot

The maximum deformation within the flanges, observed to be in the lower flange, was recorded. The plot shows a linear increase in vertical deformation with lower load levels. At around F_A = 8000kN, the trend begins to shift indicative of yielding of the material at the location. The deformation begins to increase at a much steeper rate beyond this point until a failure point at the ultimate stress is reached. It is evident that the ultimate failure of the connection occurs at a much higher load than the ULS and opening loads. Figure 7.20 shows the plastic strain development in the same node. The last plotted strain value is 22% plastic strain at F_A =11374.8 kN.

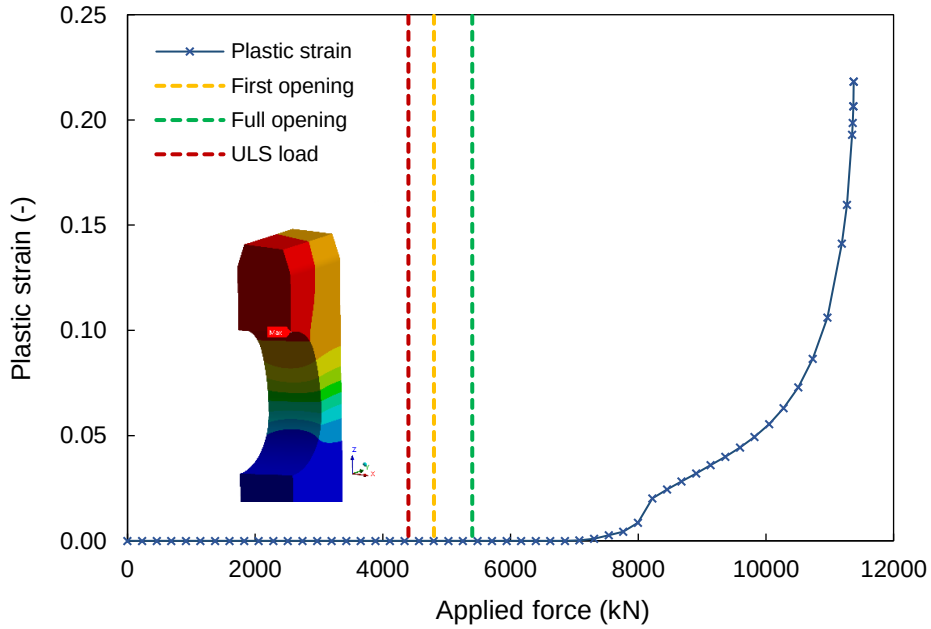

Figure 7.20: External load vs Plastic strain

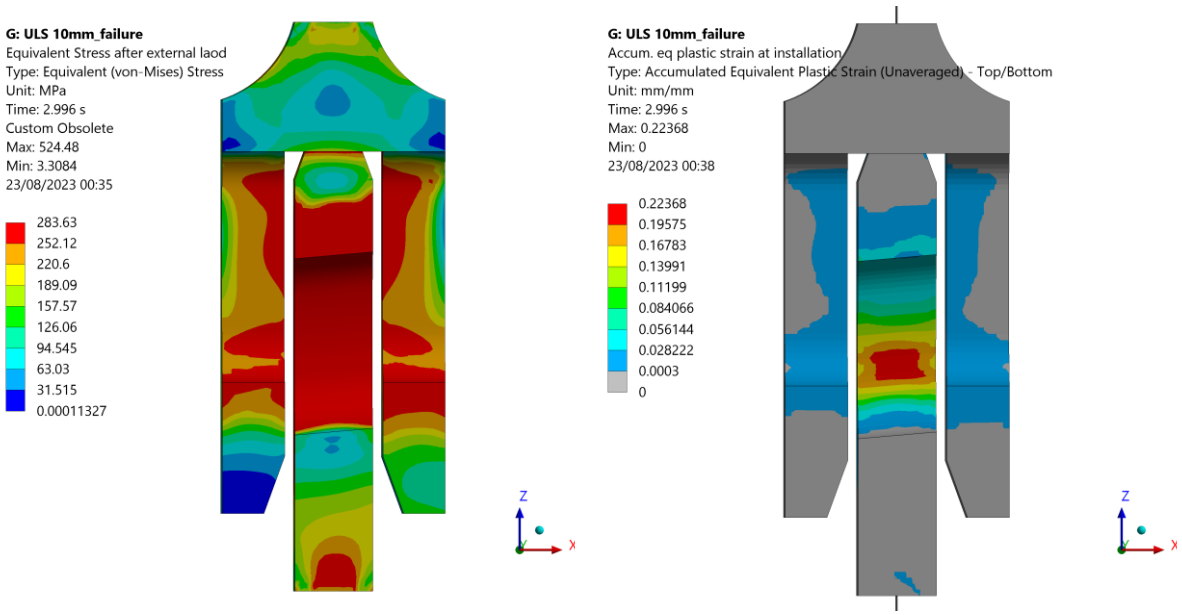

(a) (b)

Figure 7.21: (a) von-Mises stress and (b) plastic strain distribution at failure

The plots in Figure 7.21 show the region that experiences highest stress and the highest plasticity is in the lower flange, specifically at the location of the cross section with the smallest net section area. This location has the smallest area to withstand the loading and therefore is expected to be critical.

7.3.5 Discussion of the connection under external load

The results show that the connection can withstand the ULS loadcase used in this study. Excessive yielding and plasticity are not seen. The connection also only opens beyond the ULS load. The failure of the connection also occurs at a much higher load than the ULS load. This shows that the connection is still safe to operate even after opening.

7.4 Sensitivity analysis

7.4.1 Friction coefficient sensitivity

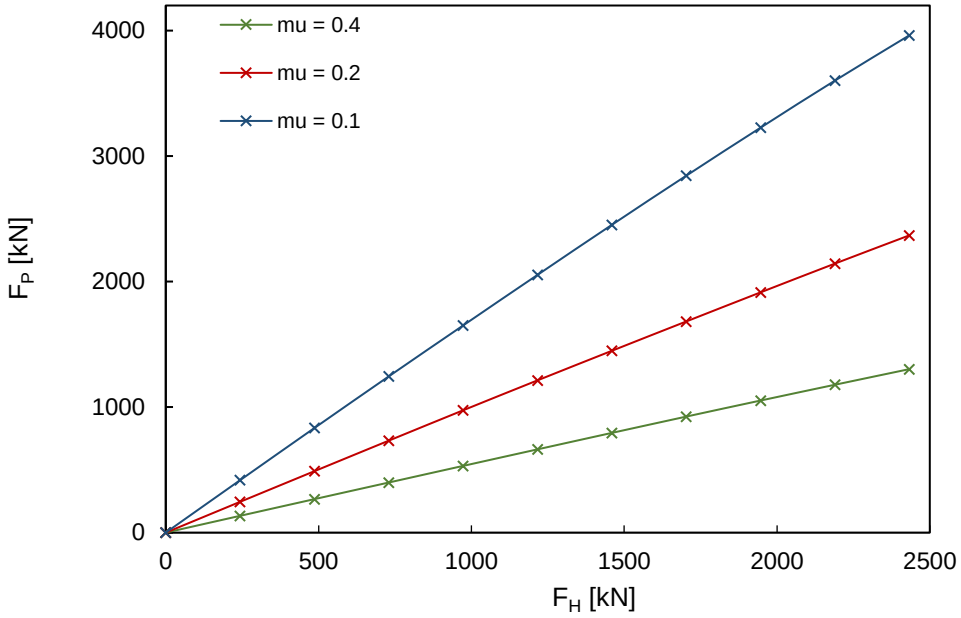

Figure 7.22: Vertical preload generation for various friction coefficients

As discussed in section 4.3, the behaviour of the connection is dependent on the coefficient of friction between the contact surfaces. Therefore, an analysis is done to investigate the sensitivity towards various friction coefficients. The static coefficients of friction defining the contact surfaces in the FE model shown in section 6.3.4 are changed. Figure 7.22 shows the sensitivity of the level of vertical preload achieved using the same horizontal load. It can be seen that a larger vertical preload is generated with smaller friction coefficients. This was expected from the analytical calculations in section 4.5 that showed a greater mechanical advantage with smaller friction coefficients as less energy is lost through friction. This shows that the connection is sensitive to friction coefficients and achieving lower friction coefficients are advantageous in providing a greater mechanical advantage.

7.4.2 Sensitivity to various levels of initial preload

The sensitivity of the connection to various levels of preloading is shown in Figure 7.23 and Table 7.4. The base case is when a horizontal preload is applied to the dowel which results in a vertical preload = 100% ULS segment load. This is to analyse how the connection will behave if this level of preload is not achieved.

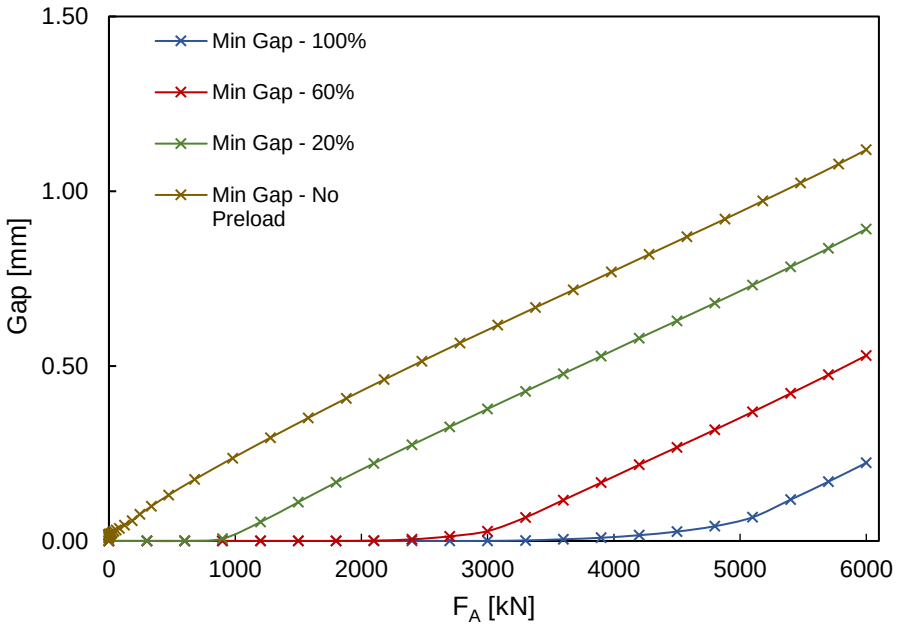

Figure 7.23: Minimum gaps for various preload levels

Table 7.4: Opening load for various preload levels

Preload level %	Load at first opening [kN]	Load at full opening [kN]
100	4800.00	5400
60	3300.00	3600.00
20	1200.00	1400.00
0	0.00	0

It can be seen from the table and the plot that lower levels of preload causes the connection to open at smaller loads. It is also visible from the graph that higher levels of preload results in a more gradual opening of the structure. The connection is therefore sensitive to the level of initial vertical preload. Therefore, a sufficient horizontal load must be applied onto the dowel during installation to guarantee that the connection has sufficient resistance.

8 Fatigue assessment

8.1 Introduction

Offshore WTG are susceptible to fatigue failure because they are exposed to a significant source of quasi-periodic excitation from wind loading (and wave loading that is not included in this report). For this assessment, an SN curve-based approach is taken based on DNV-RP-C203 [44].

8.2 Fatigue damage accumulation

As there are no welded details in the connection, it is assumed that the base material is the most critical. Hence, the fatigue failure mode of interest according to DNV-RP-C203 is the fatigue crack growth from a surface irregularity or notch into the base.

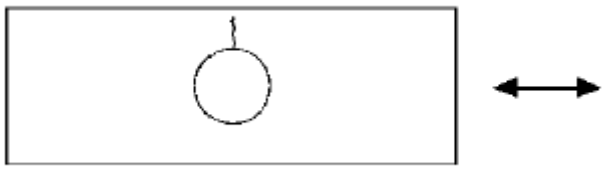

Figure 8.1: Fatigue crack growth on base material [44]

The fatigue life may be calculated based on the S-N fatigue approach under the assumption of linear cumulative damage (Palmgren-Miner rule) [44] .

$$D = \sum_{i=1}^{k} \frac{n_i}{N_i} = \frac{1}{\bar{a}} \sum_{i=1}^{k} n_i (\Delta\sigma)^m \leq \eta = \frac{1}{DFF}$$

where:

D = accumulated fatigue damage

$\bar{a}$ = intercept of the design S-N curve with the log N axis

m = negative inverse slope of the S-N curve

k = number of stress blocks

n_i = number of stress cycles in stress block i

N_i = number of cycles to failure at constant stress range Δσi

η = usage factor

DFF = design fatigue factor.

The Markov matrix approach is used. The Markov Matrix provides n_i, for each stress block. For the calculation of accumulated fatigue damage, the stress range $\Delta\sigma$ is found through FE as follows based on peak stress.

8.3 FLS loads

The FLS load spectrum was provided by C1 Connections for the same reference loadcase. It is a Markov matrix of 453 entries of mean values of bending moment acting on the connection, the moment range and the associated number of cycles experienced of this mean value. The full Markov matrix and all the calculations for this chapter is provided in Appendix D: Markov Matrix. The FLS load spectrum is presented graphically in Figure 8.2.

Table 8.1: Markov Matrix

	Mean Moment [kNm]	Moment Range [kNm]	Cycles
0	-625805.6452	17614.19355	290.06
1	-591942.7419	17614.19355	1139.9
2	-558066.129	17614.19355	5141.4
3	-524189.5161	17614.19355	98348
4	-490312.9032	17614.19355	470350
5	-456436.2903	17614.19355	1884000
6	-456436.2903	52842.58065	13077
7	-456436.2903	88070.96774	16983
8	-456436.2903	123297.9839	13733
…	…	…	…
451	492012.9032	52842.58065	878.78
452	525889.5161	17614.19355	84653
453	559766.129	17614.19355	3985.6

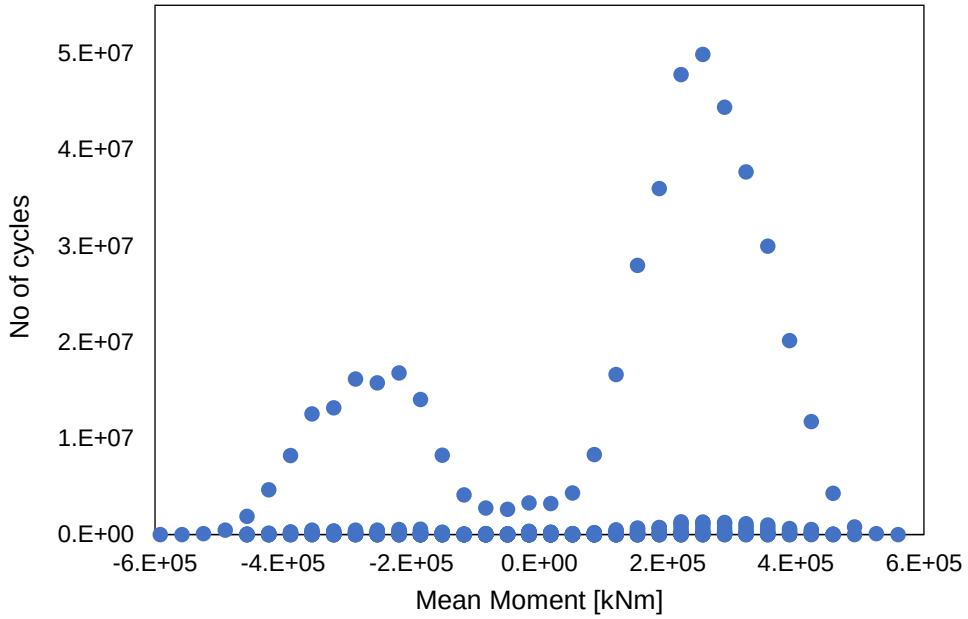

Figure 8.2: FLS load spectrum

The scaling of the load spectrum was done through the same procedure as with the ULS loads in Appendix A: ULS and FLS load calculations. For this study, the effect of wind load alone is taken into account for the scaled load spectrum and wave loading is not considered.

The maximum and minimum axial load per segment is calculated:

$$F_{max} = F_{mean} + 0.5\,F_{range} \qquad F_{min} = F_{mean} - 0.5\,F_{range}$$

The minimum and maximum of the force range spectrum is used as the load envelope for FE analysis.

$$\max(F_{max}) = 2242\ \text{kN} \text{ and } \min(F_{min}) = -2304\text{kN}$$

The motivation behind this is to ensure the full load spectrum is represented in the stress transfer function. The stress response of the structure to this fatigue load is analysed in FE.

8.4 Identification of critical location for fatigue

Fatigue cracks propagate perpendicular to the largest principal stress range, therefore the region that experiences the largest principal stress range is analysed.

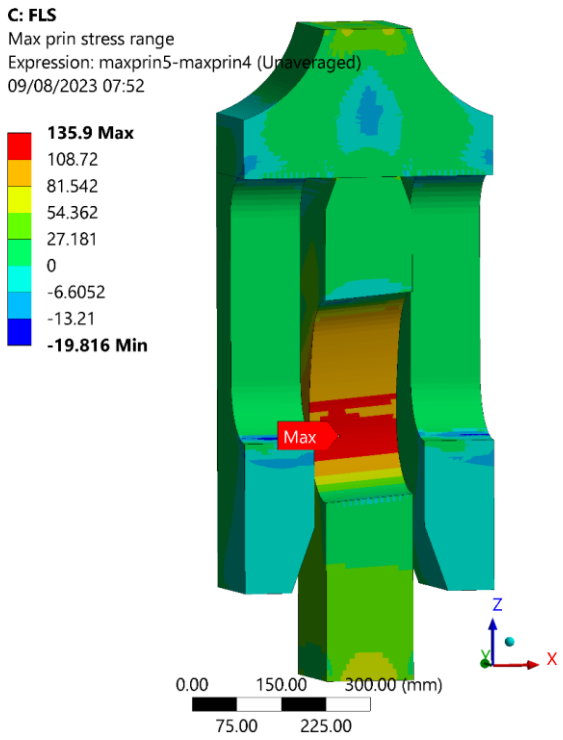

Figure 8.3: Maximum Principal Stress range in connection

As identified in the contour plot in Figure 8.3, the node that experiences the largest stress range under the load envelope is in the lower flange, which is consistent to other wedge connection designs [8]. The principal stresses from this node under the external load is shown in Figure 8.4. In order to calculate the σ_{max} and σ_{min} a linear fit of the stresses is used. This stress transfer function provides the stress response in the connection for a certain external load. The parameters used for the approximation is shown in

Appendix D: Markov Matrix. The stress transfer function along with the principal stresses at the critical node is plotted in Figure 8.4.

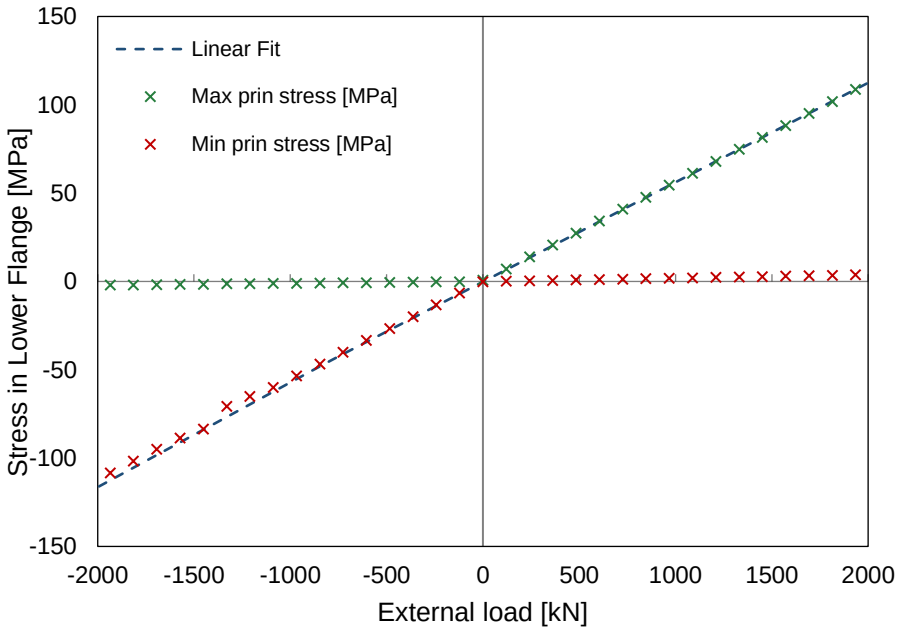

Figure 8.4: Linear approximation of stress curve alongside principal stresses in critical node

Using the linear fitted stress transfer function, the response in the structure at every external load in the Markov matrix is calculated.

Table 8.2: Maximum and minimum stress found using the stress transfer function

	F_{max} [kN]	σ_{max} [MPa]	F_{min} [kN]	σ_{min} [MPa]	Cycles $[n_i]$
0	-2211.464331	-128.83	-2274.6	-132.54	290.06
1	-2090.091918	-121.69	-2153.23	-125.41	1139.9
2	-1968.670367	-114.55	-2031.8	-118.26	5141.4
3	-1847.248815	-107.41	-1910.38	-111.12	98348
4	-1725.827263	-100.27	-1788.96	-103.98	470350
5	-1604.405712	-93.13	-1667.54	-96.84	1884000
6	-1541.272401	-89.41	-1730.67	-100.55	13077
7	-1478.139091	-85.70	-1793.81	-104.27	16983
8	-1415.008238	-81.99	-1856.94	-107.98	13733
…	…	…	…	…	…
451	1858.187074	104.16	1668.787	93.52	878.78
452	1916.475315	107.43	1853.342	103.88	84653
453	2037.896867	114.25	1974.764	110.70	3985.6

8.5 Multidirectional fatigue analysis

If there is a significant shear stress range during loading this will have to be combined with the principal stresses in a multidirectional fatigue analysis.

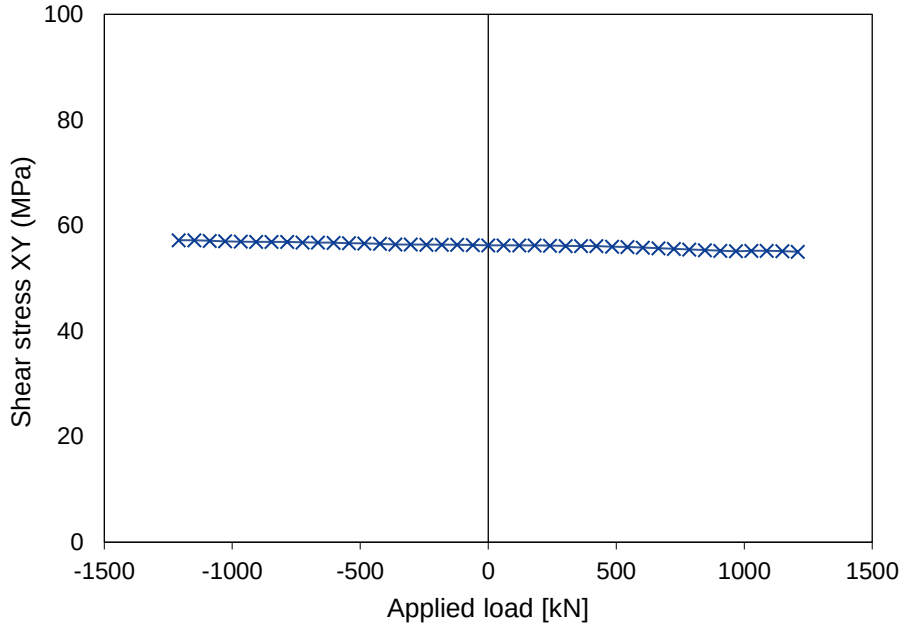

Figure 8.5: Shear stress at the critical node

However, it can be seen in Figure 8.5 that the shear stress during the loading is constant, meaning that the experienced stress range is negligible.

8.6 Fatigue damage calculation

For regions in base material not significantly affected by residual stresses due to welding or cold-forming, the stress range can be reduced if part of the cycle is in compression using the following reduction factor [44]:

$$f_m = \frac{\sigma_t + 0.6|\sigma_c|}{\sigma_t + |\sigma_c|}$$

where:

σ_t= maximum tension stress where tension is defined as positive

σ_c = maximum compression stress where compression is defined as negative

fm is 1.0 when the material is in tension during the entire stress cycle, 0.8 when it is subject to zero-mean stress, and 0.0 when it is in compression during the entire stress cycle. Detail category B1 is selected for S-N curves in seawater with cathodic protection, the properties of which are shown below.

Table 8.3: S-N curve for base material in seawater with cathodic protection [44]

SN Curve	$N \leq 10^6$ cycles		$N \geq 10^6$ cycles		Fatigue limit at 10^7 cycles
	m1	log a_1	m2	log a_2	
B1	4	14.917	5	17.146	106.97

The basic design S-N curve is given as:

$$\log N = \log \bar{a} - m \log \Delta\sigma$$

Where:

N = predicted number of cycles to failure for stress range Δσ

$\Delta\sigma$ = stress range [MPa]

m = negative inverse slope of S-N curve

$\log \bar{a}$ = intercept of the design S-N curve with the log N-axis by S-N curve.

The calculation procedure for entry 451 is shown below:

The reduction factor: $f_m = 1.0$

The stress range:

$$\Delta\sigma = \sigma_{max} - \sigma_{min} = 10.64\ MPa$$

For N ≤ 10^6 cycles, m_1=4 and $\log \bar{a}$ =14.917:

$$\log N = 14.917 - 4 * \log 10.64$$

$$N = 6.45 * 10^{10} > 10^6$$

For N ≥ 10^6 cycles, m_2 =5 and $\log \bar{a}$ =17.146

$$\log N = 17.146 - 5 * \log 10.64$$

$$N = 1.03 * 10^{12}\ cycles$$

The fatigue damage under this stress range is:

$$\frac{n_i}{N_i} = 8.55 * 10^{-10}$$

The same procedure is carried out for all the entries in the Markov Matrix. The total fatigue damage can be calculated:

$$D = \sum_{i=1}^{k} \frac{n_i}{N_i} = 0.013 \leq \eta = \frac{1}{DFF}$$

The design fatigue damage

$$D * DFF = 0.013 * 3 = 0.038 = 3.8\%$$

This is a very low level of damage and the structure is safe against the given fatigue loads.

8.7 Discussion on the fatigue resistance of the connection

The fatigue verification of the connected assisted by FE shows a low level of fatigue damage in the structure. The location of critical fatigue failure is as expected, occurring in the machined hole of the lower flange. In order to improve the fatigue prediction of the structure, a Markov matrix of the loads experienced by the structure underwater should be generated, as this analysis was performed on a scaled load case from C1 Connections. This allows for the influence of additional cyclic loading such as wave loading to be accounted for.

9 Conclusion and Recommendations

With the continued increase in scale of offshore wind projects, there is an avenue for research to reduce the sizes of MP foundations – the most commonly used WTG support structure. The aim of this thesis was to design an underwater connection between a MP and TP for offshore WTGs. The main objective was to investigate the structural behaviour of this connection. Through this study, a novel connection design has been developed and its behaviour examined through analytical hand calculations and numerical analysis. The conclusions of this research are outlined below along with some recommendations for future research.

9.1 Conclusions

The designed connection offers a notable advantage in terms of ease of installation, eliminating the need for traditional bolted connections or grouted connections. The connection raises important considerations related to corrosion protection due to the corrosive environments it will be exposed to. This study concluded that sacrificial anode systems are the ideal option for CP as they are easy to be installed, require less maintenance and does not need a continuous power supply. The investigation also highlighted that material selection plays a critical role in ensuring the longevity of the connection. With this in mind, structural steel has been chosen for all components to mitigate galvanic corrosion risks associated with bimetallic contact. Due to the challenges with maintenance and inspection, the structure is designed for a design lifetime of 30 years without any inspection.

The connection demonstrated good resistance against both the ULS and FLS load case investigated. The inclined dowel transforms a horizontal actuation load into a vertical preload between the. The connection behaviour is sensitive to the level of preload between the flanges, opening at lower external loads with lower levels of preload. The primary path to transfer tensile loads is through the reduction of this preload, as shown in the FEA results. This load path is favoured as the dowel does not take the full load fluctuation if there is sufficient preload.

The connection is also observed to experience a 7% loss of preload after installation. Preload loss is an inevitable phenomenon in many connections and this is assumed to be acceptable as the magnitude remains low. The relaxation occurs immediately after pretensioning and is predictable and therefore can be accounted for in the design. Based on the FE results, the main reason behind the loss of preload is due to the elastic deformation of the flanges after installation. Other contributing factors include the sliding out of the dowel and the increase in plastic strains within the structure.

It is beneficial to preload the connection such that the vertical preload between the flanges is equal to the ULS load. This ensures sufficient contact stress between the two flanges to transfer the external ULS load through the primary load path. The connection has a mechanical advantage of 1.95, requiring a horizontal load equal to only 51.3% of the ULS segment load in order to achieve this. The connection can withstand the installation force required without indicating excessive yielding and plasticity. Loads are transferred through the secondary path – through the dowel in shear – beyond the ULS load level, if it is preloaded to 100% of the ULS load. It also handles compressive loads effectively as they are simply transferred directly through the flanges.

The connection can effectively transfer the external loads even after it has opened. It also opens gradually, due to the uneven contact pressure distribution after preloading. The initial opening occurs at a load higher than the ULS load. The full opening of the structure occurs after the vertical preload between the flanges has been exhausted which corresponds to load transfer through the secondary load path. The ultimate limit strength and failure of the connection is governed by the yielding of the lower flange.

Another major benefit of the connection is its fatigue resistance. It showed a very low fatigue damage level of 3.8% for the given FLS loads. The preloading mechanism ensures that the dowel does not experience the load fluctuations under low levels of cyclic loading which are relevant for fatigue failure. While this may indicate a need for design optimisation, it is important to consider that wave loading was not taken into account in the fatigue calculation.

9.2 Recommendations for future research

These recommendations for future research constitute a framework to further enhance the understanding, applicability, and practicality of the developed underwater connection for offshore WTGs.

Experiments should be conducted out in order to validate the numerical results found in this study. A segment test can provide more insight into the structural behaviour of the connection. Experiments should also be carried out to investigate the impact of the presence of seawater and coating on the connection on the friction coefficient between contact surfaces.

The effect of imperfections and a sensitivity study on tolerances should also be performed as these can greatly impact the overall structural behaviour. Tolerances relating to misalignment of the flanges and dowel as well as general imperfections within the structure such as waviness, eccentricities, out of roundness and local dimples should be investigated.

Only the effect of wind loads were taken into account for ULS and FLS load case. In reality, wave loads are present but was assumed that the order magnitude was low to omit for the purposes of this study. The impact of the cyclic nature of the wave loading and its influence on the fatigue performance of the connection should also be studied. Furthermore, in this thesis, a static analysis was performed. It's important to note that both wave and wind loads are dynamic in nature. This highlights the need for a dynamic analysis to assess the significance of the dynamic nature of the loads.

It was assumed that the dowel is not coated but corrosion protection is installed. The behaviour of the sensitive contact surfaces long term in seawater should be experimentally studied. The efficacy and long-term protection provided by CP systems should also be investigated in order to reach conclusions regarding coating and CP systems to be used.

The soil structure interaction of the connection, as it is proposed to be positioned very close to the seabed should also be investigated. This is because, in this project, the exact elevation of the connection was not defined. This was because of a lack of information regarding soil and wave loading that has already been discussed. The most optimal elevation should be found in order to balance the weight split between an MP and TP based on installation vessel capacities.

In order for the connection to be installed and preloaded, heavy installation machinery will be required. The design of this machinery and any other requirements such as support railings and cranes, ROVs etc. were not studied in this project. With the heavy tools required for the installation, it will be expensive to install the connection, especially at the start prior to mass manufacturing. A cost estimation and comparison to traditional connection methods should be performed.

References

[1] W. Musial and S. Butterfield, 'Future for Offshore Wind Energy in the United States: Preprint', 2004. [Online]. Available: http://www.osti.gov/bridge

[2] M. Bošnjaković, M. Katinić, R. Santa, and D. Marić, 'Wind Turbine Technology Trends', *Applied Sciences (Switzerland)*, vol. 12, no. 17. MDPI, Sep. 01, 2022. doi: 10.3390/app12178653.

[3] Wind Europe, 'Wind energy in Europe', Feb. 2018.

[4] C. Lavanya and N. D. Kumar, 'Foundation Types for Land and Offshore Sustainable Wind Energy Turbine Towers', *E3S Web of Conferences*, vol. 184, p. 01094, Aug. 2020, doi: 10.1051/E3SCONF/202018401094.

[5] H. E. Demirci, · Saleh Jalbi, and · Subhamoy Bhattacharya, 'Liquefaction effects on the fundamental frequency of monopile supported offshore wind turbines (OWTs)', doi: 10.1007/s10518-022-01360-9.

[6] B. Handley, D. Marshall, and C. Coon, *Principles of Engineering*. 2011.

[7] K. E. Y. Creusen, 'Design and analysis of a wedge connection for offshore foundations', 2017. [Online]. Available: http://repository.tudelft.nl/.

[8] K. E. Y. Creusen, G. Misios, J. S. Winkes, and M. Veljkovic, 'Introducing the C1 Wedge Connection', *Steel Construction*, vol. 15, no. 1, pp. 13–25, Feb. 2022, doi: 10.1002/stco.202100039.

[9] P. Schaumann and M. Seidel, 'Failure analysis of bolted steel flanges', *Structural Failure and Plasticity*, pp. 507–512, 2000, doi: 10.1016/b978-008043875-7/50211-2.

[10] G+ Global Offshore Wind, *Case study on reducing manual handling and ergonomics related incidents in the offshore wind industry*. 2020.

[11] N. I. Tziavos, H. Hemida, N. Metje, and C. Baniotopoulos, 'Grouted connections on offshore wind turbines: A review', *Proceedings of the Institution of Civil Engineers: Engineering and Computational Mechanics*, vol. 169, no. 4, pp. 183–195, Dec. 2016, doi: 10.1680/jencm.16.00004.

[12] R. Mo, M. Li, and H. Kang, 'Transient behaviour of grouted connections of offshore wind turbines subject to ship impact', *Applied Ocean Research*, vol. 76, pp. 159–173, Jul. 2018, doi: 10.1016/J.APOR.2018.05.006.

[13] I. Lotsberg, 'Structural mechanics for design of grouted connections in monopile wind turbine structures', *Marine Structures*, vol. 32, pp. 113–135, Jul. 2013, doi: 10.1016/j.marstruc.2013.03.001.

[14] N. Dedić, 'Analysis of Grouted Connection in Monopile Wind Turbine Foundations Subjected to Horizontal Load Transfer', 2009.

[15] M. L. A. Segeren, E. M. Lourens, A. Tsouvalas, and T. J. J. Van Der Zee, 'Investigation of a slip joint connection between the monopile and the tower of an offshore wind turbine', *IET Renewable Power Generation*, vol. 8, no. 4, pp. 422–432, 2014, doi: 10.1049/iet-rpg.2013.0163.

[16] S. Suur and F. Hengeveld, ‘Borssele V slip joint connection: design, certification and installation of the world’s first full-size submerged slip joint’, *Steel Construction*, vol. 15, no. 3, pp. 152–159, Aug. 2022, doi: 10.1002/STCO.202100038.

[17] A. Cabboi, M. Segeren, H. Hendrikse, and A. Metrikine, ‘Vibration-assisted installation and decommissioning of a slip-joint’, *Eng Struct*, vol. 209, Apr. 2020, doi: 10.1016/j.engstruct.2019.109949.

[18] S. Thomsen and M. Troels, ‘IQPC 2018 Challenges in using bolted connections for large subsea wind structures’, 2018.

[19] Pipelie Technology Journal, ‘Snam and Enagas Vetting the Feasibility of Underwater Gas Pipeline | Pipeline Technology Journal’, 2022. https://www.pipeline-journal.net/news/snam-and-enagas-vetting-feasibility-underwater-gas-pipeline (accessed Feb. 21, 2023).

[20] Bureau of Safety and Environmental Enforcement, ‘Connector and Bolt Failures Safety Alert’, 2016, Accessed: Apr. 10, 2023. [Online]. Available: https://www.bsee.gov/safety-alerts/safety/safety-alert-318-connector-and-bolt-failures

[21] DNV GL and T. Hartvigsen, ‘Study on bolt incidents ’, 2019. Accessed: Apr. 10, 2023. [Online]. Available: www.dnvgl.com

[22] B. Ripsch and K. Henkel, ‘Assembling bolted joints under water: influence of a surrounding medium on bolt preload and slip factor’, *ce/papers*, vol. 4, no. 2–4, pp. 131–140, Sep. 2021, doi: 10.1002/CEPA.1272.

[23] M. P. Nijgh, ‘Loss of preload in pretensioned bolts’, 2016.

[24] J. Łabanowski, D. Fydrych, and G. Rogalski, ‘UNDERWATER WELDING-A REVIEW’, 2008, doi: 10.2478/v10077-008-0040-3.

[25] P. Vashishtha, R. Wattal, S. Pandey, and N. Bhadauria, ‘Problems encountered in underwater welding and remedies-a review’, 2022, doi: 10.1016/j.matpr.2022.04.634.

[26] D. Fydrych, G. Rogalski, and J. Łabanowski, ‘Problems of Underwater Welding of Higher-Strength Low Alloy Steels’, no. 5, 2014.

[27] DNV AS, ‘DNV-RP-0416: Corrosion protection for wind turbines’, 2016.

[28] DNV AS, ‘DNV-ST-0126 Support structures for wind turbines’, 2021.

[29] ‘EN 1993-1-4: General rules- Supplementary rules for stainless steels’.

[30] DNV AS, ‘DNV-OS-C101: Design of offshore steel structures, general-LRFD method’, 2019.

[31] American Bureau of Shipping, ‘Guidance Notes on: Cathodic Protection of Offshore Structures’, 2018.

[32] M. Langøy, ‘REVIEW OF STRUCTURAL CONNECTIONS OF DISSIMILAR METALS-PREVENTION OF GALVANIC CORROSION; PRACTICE AND EXPERIENCE Z-Pt-201 CLASSIFICATION OPEN CLIENT REF’, 2021.

[33] National Physical Laboratory, ‘Bimetallic Corrosion’, 2020, Accessed: Mar. 20, 2023. [Online]. Available: www.npl.co.uk/electrochemistry

[34] P. J. Blau, ‘The significance and use of the friction coefficient’, *Tribol Int*, vol. 34, no. 9, pp. 585–591, Sep. 2001, doi: 10.1016/S0301-679X(01)00050-0.

[35] *CRC Handbook of Physical Quantities*. 1997.

[36] H. Nolle and R. S. H. Richardson, 'STATIC FRICTION COEFFICIENTS FOR MECHANICAL AND STRUCTURAL JOINTS', Clayton, 1973.

[37] R. J. M. Pijpers and H. M. Slot, 'Friction coefficients for steel to steel contact surfaces in air and seawater', in *Journal of Physics: Conference Series*, IOP Publishing Ltd, Oct. 2020. doi: 10.1088/1742-6596/1669/1/012002.

[38] 'EN 1993-1-8: Design of steel structures - Part 1-8: Design of joints'.

[39] R. Nykänen, 'Simulation of Bolted Joint with Frictional Contacts'.

[40] Y. Zhu and R. Fellow, 'Best Practices for Contact Modeling using ANSYS'.

[41] 'EN 10025-3_2019: Hot rolled products of structural steels - Part 3: Technical delivery conditions for normalized/normalized rolled weldable fine grain structural steels'.

[42] DNV AS, 'DNV-RP-C208: Determination of structural capacity bynon-linear finite element analysis methods', 2019. [Online]. Available: www.dnvgl.com.

[43] M. Scheerer, M. Stubenrauch, J. Persson, O. Drescher, and S. Appel, 'ANALYSES AND TESTING OF THE THERMO-MECHANICAL BEHAVIOUR OF CRYOGENIC COMPOSITE PROPELLANT FEED LINES', 2014. [Online]. Available: https://www.researchgate.net/publication/277714239

[44] DNV AS, 'DNV-RP-C203: Fatigue design of offshore steel structures', 2019.

[45] A. F. Mohamed and A. F. Mohamed, 'Finite Element Analysis for Stresses in Thin-Walled Pressurized Steel Cylinders', *Int J Sci Eng Res*, vol. 9, no. 3, 2018, [Online]. Available: http://www.ijser.org

Appendix A: ULS and FLS load calculations

In order to determine the design loads, a typical base case provided by C1 connections based on the following wind turbine dimensions is generated:

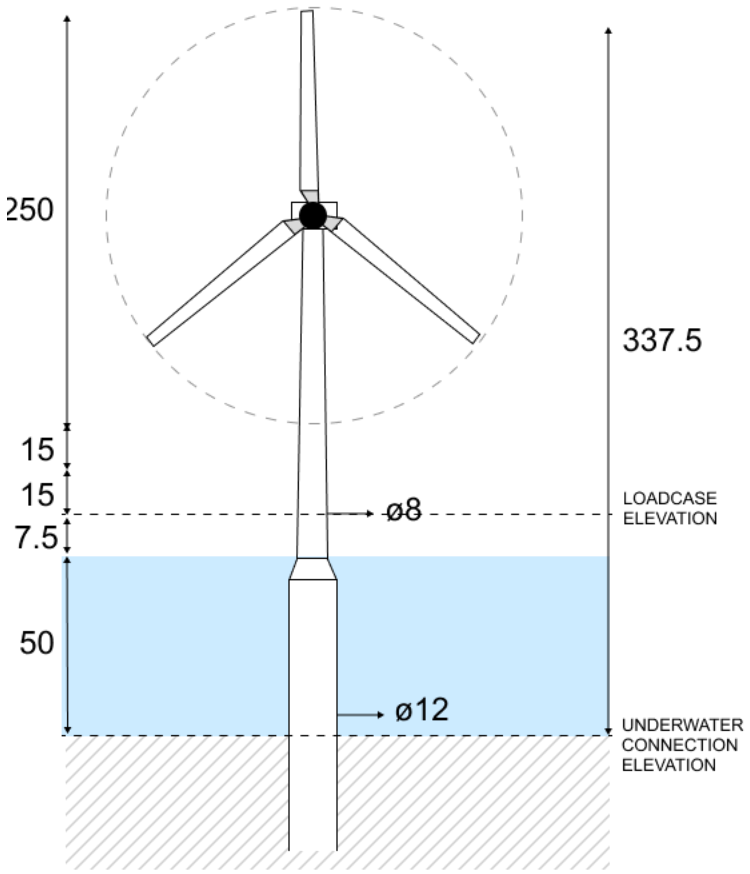

Figure A.1: WTG dimensions

Table A.1: Dimensions and Design Loads on WTG

Specification	Value
Rotor diameter	250m
Rotor clearance	15m
Distance between nacelle and WL	162.5m
Distance between nacelle and load case elevation	155m
Load case elevation to WL	7.5m
Depth of water	-50m

Connection diameter	12m
Connection wall thickness	150mm
Design bending moment at load case elevation	900 MNm

For the purpose of this investigation, it is assumed that the connection will be loaded primarily from wind loading. Wave loading is assumed to be of an order of magnitude lower than the wind load and is neglected. The global bending moment on the connection level can be found by scaling the loads from the original case study to find the wind shear load on the nacelle of the WTG. From these dimensions and design loads, the following can be calculated:

With the design bending moment at the load case elevation known, the moment at the base of the turbine can be calculated. Shear force at top of WTG:

$$V = \frac{900\ MNm}{155m} = 5.8\ MN$$

Design bending moment at underwater MP-TP connection level:

$$5.8\ MN * 212.5m = 1232.5\ MNm$$

Typically, the design line load at the connection is used for design purposes. This can be found using the following expression:

$$Q = \frac{4M}{\pi D^2} = \frac{4 * 1232.5\ MNm}{\pi * 12^2} = 10.90\ MN/m \qquad \text{(A.1)}$$

Table A.2: Design loads at connection

Design bending moment at connection	1232.5 MNm
Design line load at the connection	10.90 MN/m

Appendix B: Mesh sensitivity

A mesh size of 10mm was used for the model. Results of a mesh sensitivity analysis is shown below:

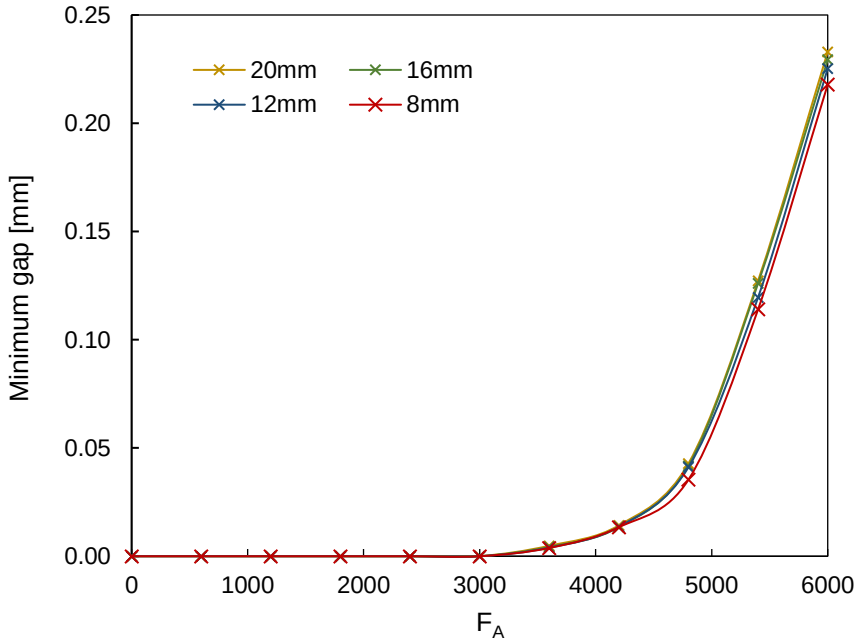

Mesh	Load at opening [kN]
8	3900
12	3900
16	3900
20	3900

The mesh size does not affect the opening load of the base case model. As local stresses are also affected by mesh quality, the unaveraged and averaged von-Mises stress is analysed for a single node in the lower flange.

Mesh size	VM	unaveraged VM
8	266.69	266.69
10	266.64	266.64
12	266.59	266.59
16	266.41	266.41
20	266.13	266.13
22	265.98	265.98

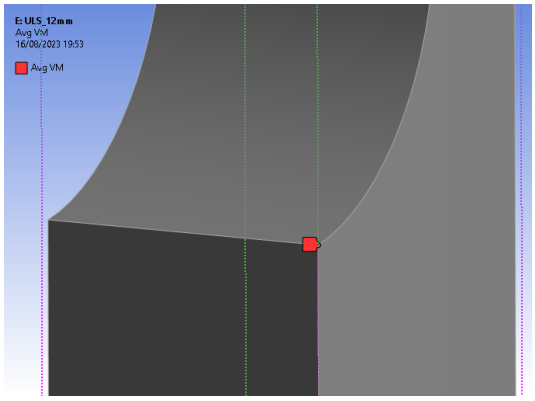

The difference between the unaveraged results and the averaged results are very low for all tested mesh sizes, which indicate a good quality mesh. The stresses also converge to a very accurate degree for mesh size 16mm and finer. Hence, the 10mm mesh used in this study produced results that are not mesh sensitive.

Appendix C: Boundary Condition Verification

C.1 Symmetric boundary condition verification

The motivation behind this study is to verify the symmetric boundary conditions used in the FE segment model. These interface boundary conditions are used to incorporate the stiffness of the overall tubular within the segment model. FE analysis for stresses in thin-walled pressurized steel cylinders was studied by Mohamed [45]. A similar study is performed here except to study the efficacy of the symmetric boundary conditions used in the segment model. A thin cylinder 75 mm internal diameter, 250 mm long with walls 2.5 mm thickness is used for this study. 5 MPa of pressure is applied to the internal faces of the cylinder. The cylinder is fixed in all directions at the top and bottom as shown in Figure C.1.

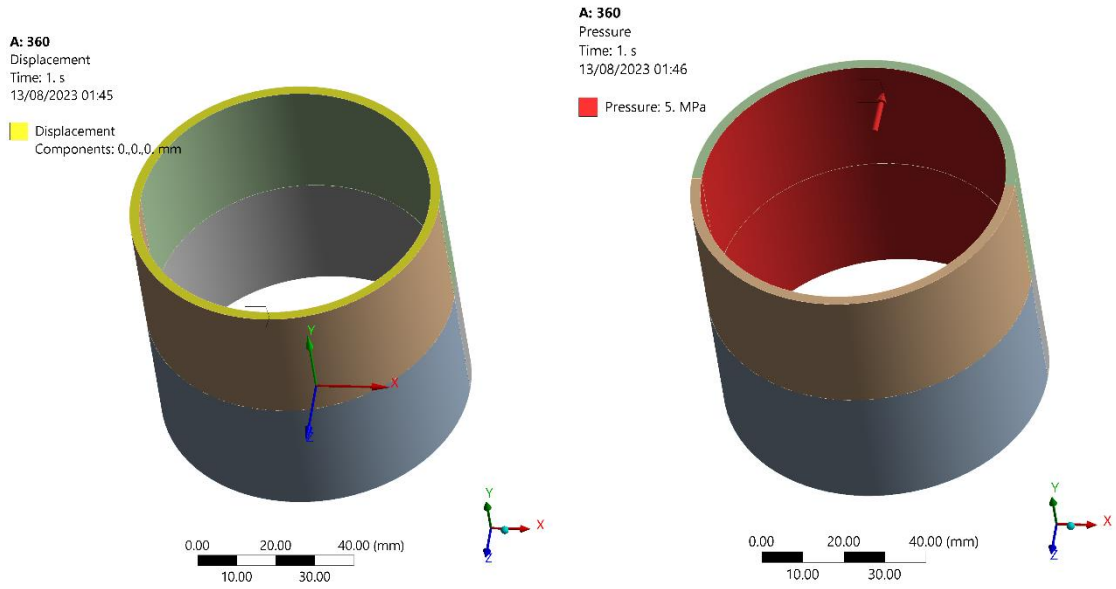

Figure C.1: Boundary conditions and pressure applied on cylinder

To study the influence of the symmetry boundary condition, two smaller models are created that utilise the displacement control at the interfaces. One model is a 180° model of the cylinder shown and a 15° segment shown below.

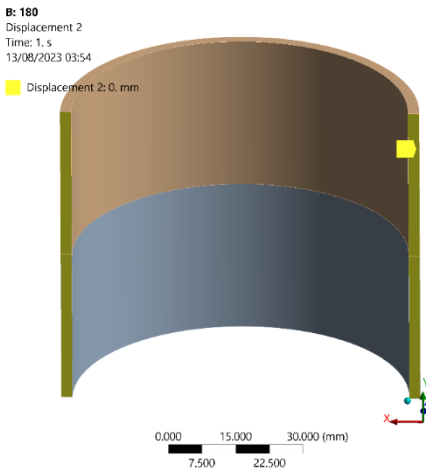

Figure C.2: 180° model of cylinder

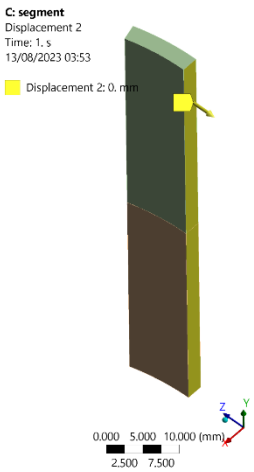

Figure C.3: 15° segment of cylinder

The deformation of the 3 models under the applied pressure is shown below. The contour plots show that the magnitude and distribution of deformation across the three models are equal.

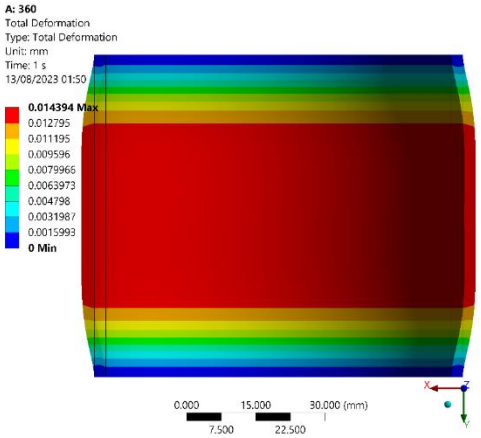

Figure C.4: Deformation of cylinder

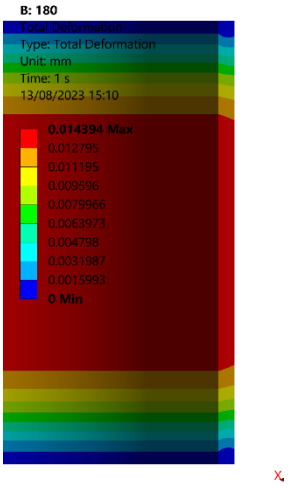

Figure C.5: Deformation of 180° model

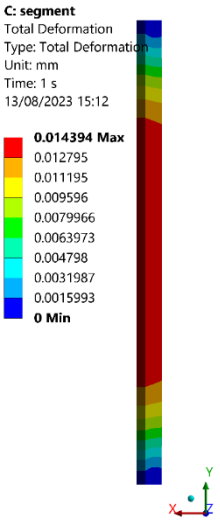

Figure C.6: Deformation of 15° model

The effect of modelling the 180° and 15° segment models without the use of displacement control in the boundaries are presented below. Hoop stress studied across the wall thickness at the same location in all 3 models. The hoop stress along the thickness is shown below.

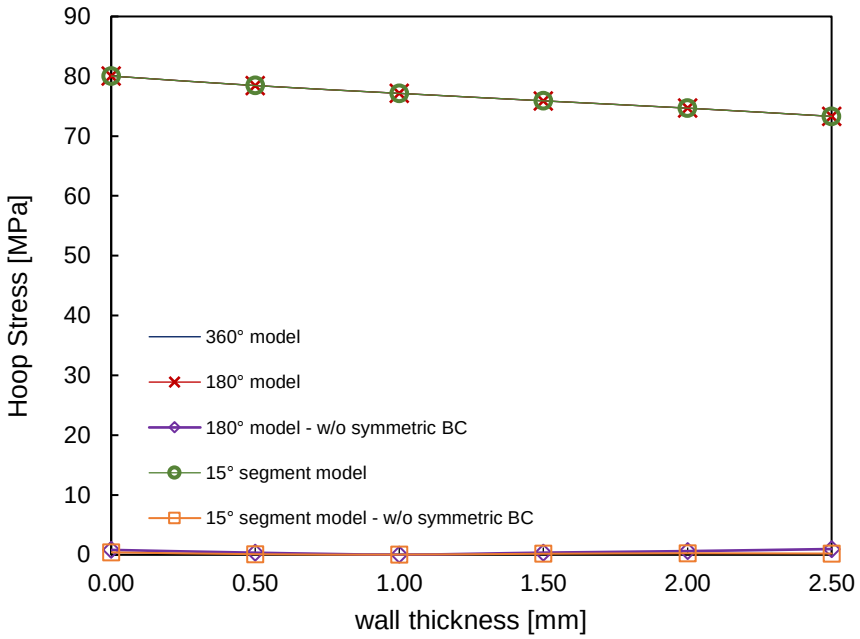

Figure C.7: Hoop stress along the wall thickness in different models

It can be seen that both the hoop stress and radial stress within the cylinder walls do not match the base model when the faces displacement are not restrained. Meanwhile when the boundary conditions are implemented, the wall stresses closely match the base model's results. The results show that the displacement control at the boundaries allow for a reaction force in the hoop and radial direction that simulates the stiffness of the complete cylinder within the smaller model. This shows that the boundary conditions used in the segment model for the underwater wedge connection incorporates the stiffness of the overall tubular connection.

C.2 Boundary condition sensitivity

As shown in Figure 6.6, the model is constrained at the bottom edge against displacement in radial and vertical direction, to prevent rigid body motion. This is necessary to ensure stability of the numerical model. However, it is important that these boundary conditions do not provide additional reaction force against the installation of the dowel. The dowel should be resisted exclusively by the symmetric boundary conditions that simulate the ring stiffness of the entire structure. To ensure this, the edge is placed 2m below the connection level so that its effect on the structure is negligible. The sensitivity of the model to this distance is checked by varying the distance of the tubular height below and above the connection.

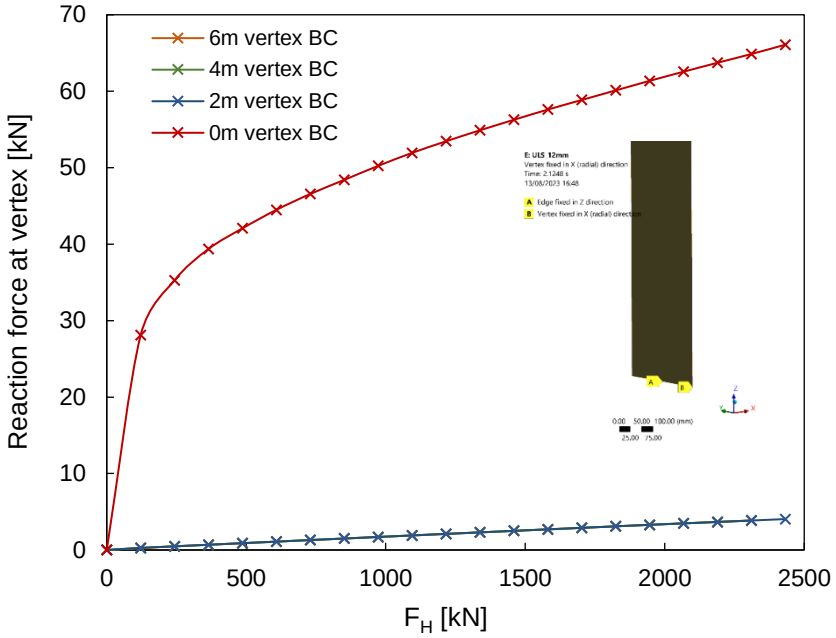

Figure C.8: Reaction force measured at the vertex

It is seen from the figure that when no distance is provided between the bottom of the connection and the boundary condition, the vertex provides a reaction force, whereas, the other models do not have a significant reaction force. This is further investigated by analysing the radial deformation of the lower flange in Figure C.9.

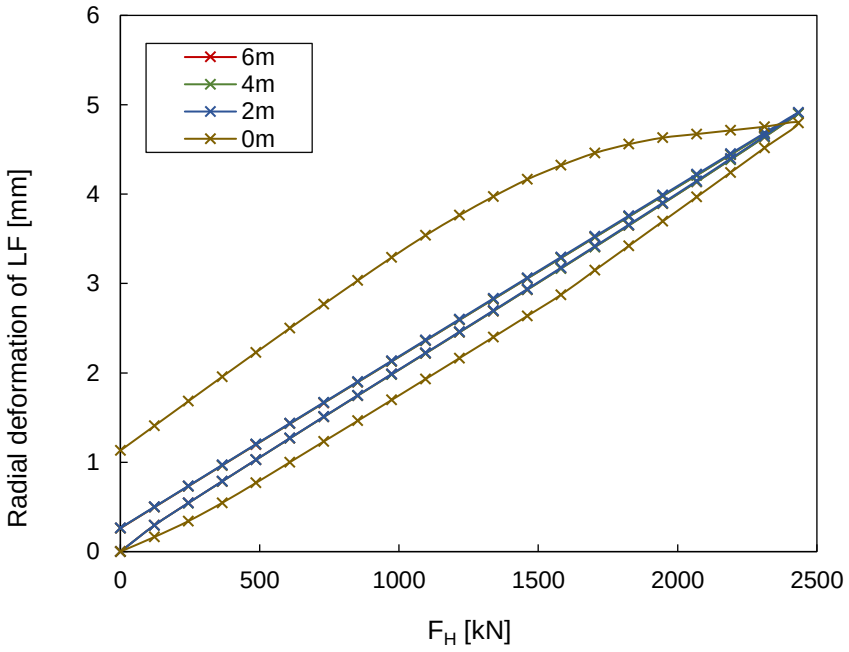

Figure C.9: Radial deformation of lower flange with various boundary lengths

The plot shows a very similar behaviour for all the models that have a clearance. It is evident that providing more than 2m clearance is not necessary. However, when no distance is given, there is a large degree of permanent deformation. Inspecting the boundary condition closer, it can be seen that

there is a development of plasticity at the region near the vertex that is restrained. This is not a realistic phenomenon and shows that a certain length of tubular should be modelled below the connection.

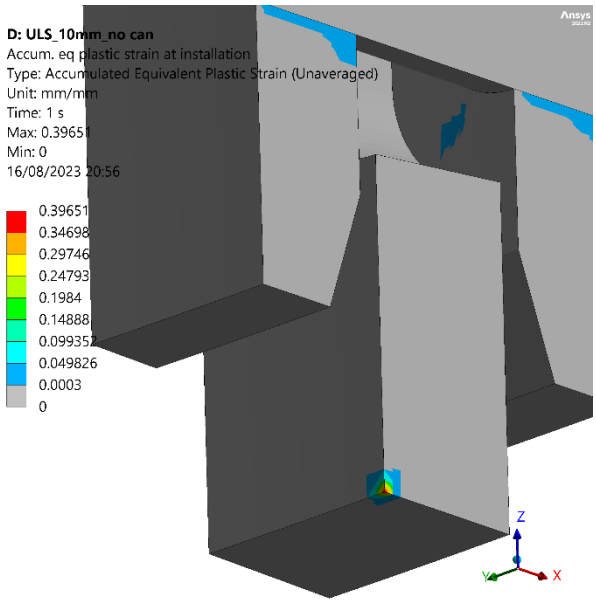

Figure C.10: Close up of restrained vertex with plastic strain developing when no tower section is modelled

Appendix D: Markov Matrix

Excel sheet is attached to this submission.